Resting-state network hubs are causally required in memory consolidation

Zengmin Li[a], Dilsher Athwal[a], Hsu-Lei Lee[a], Pankaj Sah[a,e], Patricio Opazo[a,b,c], Kai-Hsiang Chuang[a,d*]

[a] Queensland Brain Institute, The University of Queensland, Brisbane, Australia

[b] Clem Jones Centre for Ageing Dementia Research, The University of Queensland, Brisbane, Australia

[c] UK Dementia Research Institute, Centre for Discovery Brain Sciences, The University of Edinburgh, Edinburgh, UK

[d] Centre of Advanced Imaging, The University of Queensland, Brisbane, Australia

[e] Joint Center for Neuroscience and Neural Engineering, and Department of Biology, Southern University of Science and Technology, Shenzhen, Guangdong Province, P. R. China, 518055

Running title: Network hubs of memory formation

***Address correspondence to:**

Kai-Hsiang Chuang, Ph.D.

Queensland Brain Institute

The University of Queensland

Brisbane, Queensland 4072, Australia

Email: kaichuang@gmail.com

Summary

Resting-state networks (RSNs) detected by fMRI have been associated with cognitive function, providing insights to the relationship between brain and behavior. However, whether altered RSNs are epiphenomena or essential constructs of behavior remains unclear. Here we investigated whether post-encoding RSN hubs that are commonly engaged after similar tasks or integrate distributed areas into large networks are causally involved in memory consolidation. RSN changes following two types of spatial memory training in mice, allowing us to distinguish post-encoding hubs related to spatial memory, and verify their behavioral impact by hub inhibition. We found that functional connectivity with sensory areas was commonly strengthened in both tasks whereas frontal and striatal areas were influential in network integration. Chemogenetic suppression of each hub after learning resulted in retrograde amnesia. These results demonstrate causal and functional roles of RSN hubs in system consolidation and validate fMRI as a means to track this process.

Keywords: functional connectivity, brain connectome, memory consolidation, resting state network, resting-state fMRI.

Introduction

Understanding the nature of brain networks and how they are orchestrated to support cognitive functions, such as learning and memory, is fundamental in neuroscience. Based on resting-state functional magnetic resonance imaging (rsfMRI), functional connectivity (FC) measured as the statistical relationship between regional hemodynamic activities has been found to form large-scale resting-state networks (RSNs) that associate with cognition and its age-related disorders at the system level (Biswal et al., 1995; Craddock et al., 2013; Mill et al., 2017). For instance, FC correlates with and predicts memory performance and can be reshaped by learning, indicating strong behavioral relevance of the RSNs (Albert et al., 2009; Bassett et al., 2011; Kao et al., 2020; Tambini et al., 2010). The disruption of RSNs in association with cognitive impairment and neuropathology provide further evidence for the involvement of these networks in the etiology and progression in diseases (Greicius et al., 2003; Pievani et al., 2014; Yu et al., 2021). These findings have supported the use of the RSNs for the differentiation of disease biotypes, the investigation of circuit mechanisms, the identification of targets for intervention, and the creation of predictive models of disease processes (Drysdale et al., 2016; Fornito et al., 2015; van den Heuvel and Sporns, 2019; Matthews and Hampshire, 2016). However, due to the observational and correlative nature of the experimental designs, confounds in the undirected FC measures and unconstraind imaging environments, the behavior- or disease-dependent RSN changes may not be causal but rather epiphenomena that are driven by other neural pathways or alternative physiological or pathological factors (Cole et al., 2010; Drew et al., 2020; Duncan and Northoff, 2013; Gonzalez-Castillo et al., 2021). Whether an RSN or a network hub is causally required for cognition (e.g., episodic memory), such that its dysfunction leads to a disability (e.g., amnesia) while its facilitation improves performance is rarely examined (Reid et al., 2019).

Among the various considerations for improving causal inference (Reid et al., 2019), the identification and validation of a causal hub are essential. In both human and animal studies, causal areas are typically determined by prior knowledge (Kim et al., 2016). The hippocampal-cortical network, particularly between the hippocampal formation (HPF), retrosplenial cortex and medial prefrontal cortex (mPFC), has been extensively investigated using different spatial or contextual learning paradigms (Eichenbaum, 2017; Kitamura et al., 2017; Milczarek et al., 2018; Paul et al., 2009; Ranganath and Ritchey, 2012). The storage of

various forms of spatial memory trace (engram) in these areas suggests that a common network may be involved in the system consolidation of memory [ref] . However, common hubs beyond these areas are seldom explored.

A variety of network analysis methods have been developed to detect influential hubs or to infer causality from rsfMRI (for review, see (Bielczyk et al., 2019). Most approaches use graph theory, where by a brain network is simplified as nodes (brain regions) and edges (structural or functional connections) in a graph (Bullmore and Sporns, 2009). Topology measures have been used to characterize brain network changes in behavior. For example, modularity, which measures the division of nodes into connected clusters, represents network segregation, with its flexibility being associated with motor learning capability (Bassett et al., 2011). Centrality, which describes the number of edges passing a node, is important in network communication and has been found to associate with spatial memory performance (Liu et al., 2016). These findings are in line with the importance of network integration in memory processes as shown in a number of rsfMRI studies (Cohen and D'Esposito, 2016; Debas et al., 2014; Keerativittayayut et al., 2018). Despite these recent advances, however, the brain areas that are central for integrating the RSNs during memory processes remain unknown.

In general, the causal role of behavior-associated RSN hubs, and how they contribute to a behavior have not been tested. This is partly because most causal inference methods are demonstrated by computer simulations, with little empirical evidence to validate their accuracy. Non-invasive brain stimulation, such as transcranial magnetic stimulation, provides a way to verify the causal role of RSNs (Fox et al., 2012; Tambini and D'Esposito, 2020; Wang et al., 2014). Nonetheless, these techniques have poor spatial localization, are limited to cortical areas and produce unclear effects in downstream networks, making it difficult to pinpoint causal links between a structure and its connection (Bergmann and Hartwigsen, 2021). Highly targeted techniques such as optogenetics and chemogenetics in animal models provide another way to understand the relationship between brain network and behaviour. Vetere et al. (2017) demonstrated that causal hubs could be discovered by network analysis base on chemogenetic inhibition of high centrality nodes estimated from covariate *c-fos* activity networks. Importantly, fear memory consolidation could be impaired and correlated with reduced global efficiency, which reflects network integration (Vetere et al., 2017).

The discovery of RSNs in the rodent brain has provided an opportunity to interrogate their causal roles in behaviour (for review, see (Chuang and Nasrallah, 2017). Previously, we and others have found that spatial memory learning in a Morris water maze can lead to task-dependent plasticity in rodent RSNs over the days following learning (Nasrallah et al., 2016; Shah et al., 2018). As neural synchrony during the resting period plays a critical role in supporting memory consolidation (Headley and Paré, 2017), post-encoding RSN changes may be involved in consolidating or even storing a memory trace (Tambini and D'Esposito, 2020). Here, we hypothesized that two kinds of post-encoding RSN hubs are causally engaged in memory consolidation:

1) *Common network*: consolidation of a similar kind of memory involves the same RSN hubs.
2) *Network integration*: consolidation increases network integration by forming large network modules mediated by integrator hubs.

To identify the common networks, we trained mice in two versions (early and late retrieval) of active place avoidance (APA), a spatial memory task. After learning, rsfMRI data were acquired to detect behavior-induced RSN changes, followed by *in silico* hub identification. We then validated the identified hubs by silencing each hub individually during the consolidation period using inhibitory Designer Receptors Exclusively Activated by Designer Drugs (DREADDs). Our results revealed that silencing either common or integrator hubs can lead to retrograde amnesia, confirming the validity of the analysis. These findings demonstrate that RSN hubs not only reflect post-encoding plasticity but are also required for memory cosolidation, hence providing a causal and functional link between the RSN and behavior.

Results

Mice learned 1-Day and 5-Day APA tasks

APA allows spatial navigation and memory to be assessed in mice with less stress than that associated with the water maze by training them to avoid a shock zone based on spatial cues over several trials (Fig. 1A) (Cimadevilla et al., 2001; Lesburguères et al., 2016). To investigate whether similar tasks engage comparable RSNs, we conducted two kinds of APA tasks with the same five training trials but with different inter-trial intervals: one hour (1-Day APA, as the learning was completed in one day) versus one day (5-Day APA). Over five 10-min trials, the number of shocks (N_{shock}) that animals received, which represents a failure to avoid the shock zone, gradually decreased in both tasks ($F_{4, 64}$ =15.77 for 1-Day APA, $F_{1.688,27}$ = 7.83 for 5-Day APA, one-way ANOVA; Fig. 1A). Compared to the last trial of training (T5), the N_{shock} was significantly fewer than for the first three training trials, T1 ($t = 4.81$, $p < 0.0001$), T2 ($t = 4.81$, $p < 0.0001$) and T3 ($t = 3.97$, $p = 0.0002$), in the 1-Day APA. In the 5-Day APA, the N_{shock} of T5 was less than the first two training trials, T1 ($t = 4.56$, $p < 0.0001$) and T2 ($t = 3.62$, $p = 0.0005$). The time to first entrance into the shock zone (i.e., the initial avoidance time; T_{enter}) is another index of how well the memory is recalled in each trial. In the 1-Day APA, the T_{enter} was significantly longer in T5 compared to the first three training trials, T1 ($t = 2.97$, $p = 0.016$), T2 ($t = 2.93$, $p = 0.017$), and T3 ($t = 2.89$, $p = 0.018$). In the 5-Day APA, the T_{enter} in T5 was significantly longer than the first training trial ($t = 2.62$, $p = 0.034$). These results indicated successful learning in both tasks.

After learning, two sessions of rsfMRI scans were performed on post-training day 1 and 8 to examine the plasticity of the RSNs (Fig. 1B). One day after the second rsfMRI scan, a probe test was performed to assess memory retention. The N_{shock} and T_{enter} during the probe test were not significantly different from the last training trial in both 1-Day (N_{shock}: $t = 1.36$, $p = 0.18$; T_{enter}: $t = 1.23$, $p = 0.25$) and 5-Day (N_{shock}: $t = 0.82$, $p = 0.42$; T_{enter}: $t = 1.76$, $p = 0.12$) APA, indicating good memory retention in both tasks (Fig. 1A). Comparing 1-Day and 5-Day APA, no difference was found in the N_{shock} ($F_{1, 16} = 0.55$, $p = 0.47$, Two-way ANOVA) or T_{enter} ($F_{1, 16} = 1.27$, $p = 0.28$). These results demonstrate that mice could remember both APA tasks equally well after 9 days, indicating the formation of long-lasting memory.

Post-encoding RSNs change differentially over time

We measured the RSNs using an ultrafast blood oxygenation level-dependent (BOLD) rsfMRI method to increase sensitivity (Lee et al., 2019). After the data were postprocessed by an optimized pipeline to remove nuisance signal fluctuations (Chuang et al., 2019) and nonlinearly registered to the AMBMC brain template (Ullmann et al., 2013), seed-based correlation analysis was used to calculate the FC strength from the mean BOLD signals between 230 parcellated regions (supplementary Table S3), followed by Fisher's z-transformation to construct the connectivity matrix in each animal (Fig. 1B). To distinguish connections that were altered by spatial learning, we used two-sample t-tests to compare the FC matrices of the APA groups with their controls, in which animals were exposed to the APA training procedures without any foot shock as we found that random shock elicited a strong stress response (data not shown).

Fig. 2A shows the dynamics of post-encoding RSNs following two kinds of APA learning. On post-training day 1, 1-Day APA increased the long-range FC between the entorhinal cortex and motor control area (pontine nucleus), and between reward processing areas (olfactory tubercle (Tu) and dorsal anterior cingulate cortex (A24b)), but decreased the FC between the secondary somatosensory cortex (S2) and a decision-making area (medial orbital cortex (MO)), and between an emotional response area (ventral anterior cingulate cortex (A24a)), pons, and HPF. One week post APA training, the network reorganized, with increased FC among the somatosensory cortex, areas for emotional and motor responses – A24a, lateral accumbens shell (LAcbSh) and amygdala (Etkin et al., 2011; Goode et al., 2019) – and ventral entorhinal cortex (VIEnt). On the other hand, the FC between the thalamus, pons, lateral orbital cortex (LO) and somatosensory cortex decreased.

Different from 1-Day APA, 5-Day APA increased the FC mostly between the midline areas in the left hemisphere (e.g., A24a and mammillary bodies) and distributed areas in the right hemisphere, including the HPF, prefrontal cortex and sensory areas. It is worth noting that a large portion of those brain regions are in the limbic system, which has been reported in a variety of functions, including long-term memory (Catani et al., 2013; Rolls, 2015). The highly lateralized FC (12 out of 17) is consistent with studies reporting that the right hemisphere is predominant in memory processing (Metcalfe et al., 2016; Shinohara et al., 2012; Tucker et al., 1999). On post day 8, only two decreased FC between the HPF, ventral orbital cortex (VO) and a subcortical visual system, the anterior pretectal nucleus (APT), was found in the right hemisphere. No common FC between the 1-Day and 5-Day APA was observed, likely due to the drastically reduced false positive rate when calculating the overlap between two FDR-

corrected matrices.

APA learning increases network integration

To examine whether network integration was enhanced by spatial learning, graph theory analysis was applied to the t-value matrixes of two-sample tests. The global efficiency, modularity, and the size of giant component (the largest connected cluster of nodes in a network) (Vetere et al., 2017) were calculated at t-score threshold (uncorrected) from 2.0 to 3.8 (supplementary Fig. S1). To compare the overall difference of these indexes, the area under curve (AUC) was calculated (Zhang et al., 2015) and compared to the distributions of 5000 random networks. Fig. 2C shows example trends of reduced giant component with increased threshold for random networks and the real network from 1-Day APA on post day 1. Compared to random networks, both APA training, except 5-Day APA on post day 8, significantly increased the size of giant component (Fig. 2D). Interestingly, the global efficiency was found only increased in 1-Day APA post day 8 while decreased in 5-Day APA post day 8 (supplementary Fig. S1). Besides, we found that modularity is significantly higher than random networks in both APA tasks at both time points (supplementary Fig. S1). These results together indicate that the APA learning increases network integration by forming larger networks while also promotes modularity.

Significant FC seldom predicts behavior

It is generally expected that behaviorally relevant connections correlate with or predict behavioral performance. Although many studies have found association between memory performance and the FC during encoding or retrieval, little is known about the relationship with post-encoding FC. To test whether post-encoding FC can predict memory retention, we calculated Person's correlation between FC strength and N_{shock} or T_{enter} in the probe test (Fig. 2B). Only two connections on post day 8 in the 1-Day APA group correlated with behavior: between the left posterolateral cortical amygdala (PLCo) and LAcbSh ($r = 0.87$, $p = 0.0045$) and between the right primary somatosensory cortex jaw region (S1J) and inferior colliculus (IC) ($r = 0.82$, $p = 0.012$). Although several connections were enhanced in 5-Day APA, no correlation with behavior was found. The general lack of association with memory recall indicates that significant FC may not necessarily predict behavioral performance.

Identify hubs from common networks

To discover common RSNs induced by both APA tasks, the threshold for two-sample t-test

was lowered to uncorrected $p<0.05$ (Fig. 1C). Despite similar in their task designs, only a small fraction of the FC was common in both APA tasks, with 3.56% (post day 1) and 2.85% (post day 8) of the connections overlapping. To identify the causal hub, we selected the common FC predictive of behavioral performance in the probe test. Using a permutation test, imposing behavior correlation with N_{shock} (threshold at $p<0.05$) resulted in equivalent family-wise error $p < 0.05$ for common RSNs on both post day 1 and 8 (Fig. 3B). If using T_{enter} as a behavior index, the family-wise false positive rate of common RSNs on post day 1 was $p < 0.05$ while $p > 0.05$ for post day 8 (supplementary Fig. S2). Here, we chose to use N_{shock} as the primary behavior index. On post day 1 (Fig. 3A, supplementary Table S1), connections within and between the limbic areas (particularly the hippocampus and A24a) and thalamus in the left hemisphere, and the connection between the primary somatosensory and primary visual (V1) cortices in the right hemisphere predict N_{shock} (Fig. 3C). Excluding the HPF and mPFC, which are known to engaged in memory consolidation, and subcortical areas, the FC of the left primary somatosensory cortex barrel field ($S1BF_L$) had the highest behavioral correlation ($r = -0.68$), followed by the right V1 ($r = 0.57$; Fig. 3C). On post day 8 (Fig. 3B, supplementary Table S1), FC with the limbic area was less. Excluding the entorhinal and retrosplenial cortices, the right secondary somatosensory cortex ($S2_R$) had the highest behavioral correlation ($r = -0.80$, Fig. 3D). Therefore, the $V1_R$ and $S2_R$ were chosen as the targets for validation.

Identify integrator hubs

We predicted that when an integrator hub is removed (inhibited), the integration of post-encoding RSNs would be greatly impeded, leading to a breakdown of large network (giant component). The best method for hub identification would be the one which can reduce the size of giant component with the removal of fewest number of nodes. Although centrality is regarded as reflecting network integration, simulation showed that centrality is poor measure for causal inference (Dablander and Hinne, 2019). To determine the best method, we compared four centrality measures (degree centrality, closeness centrality, betweenness centrality, eigenvector centrality) and collective influence (CI), which searches for nodes that can quickly breakdown large networks in an optimal percolation model (Morone and Makse, 2015; Morone et al., 2016). We calculated the reduction of giant component in the post-encoding RSNs by removing high ranking/centrality nodes one-by-one. Fig. 4A shows an example that the normalized giant component size quickly dropped by removing nodes detected by the CI, followed by those identified by the degree centrality and betweenness centrality, while

closeness and eigenvector centrality were relatively slow. Similar trends were observed in networks from both APA groups at both time points (supplementary Fig. S3). Comparing the AUC of the giant component changes, the CI analysis resulted in the quickest collapse of giant component (Fig. 4B, supplementary Fig. S4). This indicates that CI is a better method for identifying integrator hubs.

As shown in Fig. 2A, the use of FDR-corrected threshold makes the network very sparse without a giant component, thus prohibits the use of CI analysis for hub identification (Morone and Makse, 2015; Zhu, 2018). Here, we used multiple uncorrected thresholds, $p < 0.05$, 0.01 and 0.005, to determine the averaged ranking of a node in breaking down the RNSs after 1-Day APA training. On post day 1, the top-ranking 10 nodes are mostly subcortical, including regions in the basal ganglia, midbrain and brainstem, with cortical areas in the HPF (subiculum and entorhinal cortex) and S2 of lower ranks (Table 1). On post day 8, more cortical areas (parietal association cortex, sensory and PFC) became top ranking compared to subcortical areas. Considering behavior correlation of the FC with these CI nodes, there were only a few nodes with FC predictive of memory recall (Table 2). The results show that the FC of the right caudate putamen had the highest correlation with the N_{shock} ($r = -0.79$, $p = 0.0063$), and the left LAchSh shows the highest correlation ($r = 0.95$, $p = 3.7x10^{-5}$) with the T_{enter} on post day 1. On post day 8, nodes with high behavioral correlation include the left ventromedial thalamic nucleus ($r = 0.91$, $p = 0.0015$), left primary somatosensory cortex forelimb region ($S1FL_L$; $r = 0.89$, $p = 0.0033$), right LO ($r = 0.87$, $p = 0.0045$) and right primary somatosensory cortex trunk region ($S1Tr_R$; $r = -0.84$, $p = 0.0095$). Thus, the $LAchSh_L$, LO_R, and $S1Tr_R$ were chosen as candidate hubs for validation.

Validation by DREADDs inhibition

To verify the role of selected hubs in memory consolidation, we injected AAV2/1-pSyn-hM4D(Gi)-T2A-mScarlet to transfect inhibitory DREADDs in all neurons in these areas (Fig. 1D). One month after the surgery, animals went through the 1-Day APA training. Immediately after finishing the 5 training trials, animals were administered clozapine N-oxide (CNO) by intraperitoneal (i.p.) injection, followed by drinking CNO-doped water to maintain inhibition of the targeted hubs for 7 days until one day before the probe test, allowing CNO to clear (Jendryka et al., 2019; Raper et al., 2017). In addition to a naïve group for controlling the effect of CNO, we chose one cortical, the right frontal association cortex (FrA_R), and one subcortical, the right ventral posteriomedial thalamus (VPM_R), area as negative controls. Fig. 5 shows good viral expression at the targeted areas in both experimental and control groups. We did notice

that there was some viral expression in nearby brain areas because of the brain structure property and normal diffusion, such as the $S2_R$ and $LAcbSh_L$.

Animals learned 1-Day APA successfully (Fig. 5D-G). The consistent improvement over the 5 training trials in the 2 negative control groups show that the surgery itself did not affect spatial learning (Fig. 5E, G). After receiving CNO for one week, animals in the negative control (FrA_R and VPM_R) or in the CNO control group showed intact memory recall in the probe test (Fig. 5D-G). The N_{shock} after inhibiting the $V1_R$, $S2_R$, $LAcbSh_L$ and LO_R during the consolidation period was significantly increased compared to their own last training trial (T5), while no difference was found after inhibiting a low-ranking node, the $S1Tr_R$. They also showed significantly more changes in N_{shcok} compared to the CNO control (Fig. 5H). The T_{enter} also exhibited similar trends in these groups except the $V1_R$ (supplementary Fig. S5). These results demonstrate that inhibition of the common network hubs or top-ranking integrator hubs can impair memory consolidation.

Discussion

Here we show that spatial learning leads to ongoing reorganization of RSNs and inhibition of specific hubs of post-encoding RSNs results in retrograde amnesia. This demonstrates a causal link between post-encoding RSN hubs and memory consolidation and highlights a functional significance of the RSNs in learning. We also demonstrated two hypotheses for discovering new network hubs involved in memory process. We found that FC with sensory areas, V1 and S2, were enhanced by APA training of different inter-trial intervals, whereas a prefrontal area, LO, and part of the ventral striatum, LAcbSh, were important hubs for network integration. Furthermore, network hubs identified at either 1 or 8 days following learning are effective in modulating memory formation. This suggests different roles of these hubs in memory consolidation. This is distinct from previous studies which mostly focus on networks or regions centered around the hippocampus (Goode et al., 2020; Kitamura et al., 2017; Liu et al., 2012; Milczarek and Vann, 2020; Miller et al., 2018; Sousa et al., 2019). Compared to invasive imaging, such as *c-fos* or calcium imaging, non-invasive rsfMRI allows longitudinal imaging in both animal models and humans. This could complement *c-fos* imaging of active neural populations acquired during encoding or recall (Vetere et al., 2017). Our findings contribute to the establishment of rsfMRI as a translational tool for tracking the dynamics of system-level network remodeling in cognitive processes. Combining *in vivo* imaging, network-based target identification and neuromodulation in memory formation could have great potential for the treatment of various disorders, such as post-traumatic stress disorder and dementia (Phelps and Hofmann, 2019).

We discovered new roles of sensory areas (V1 and S2) in system consolidation. Early visual cortex has been shown in consolidating visual working memory (van de Ven et al., 2012), however, its role in long-term memory consolidation has not been reported. Although the hippocampus does not directly drive primary sensory areas, replay of maze-running activity patterns during slow-wave sleep has been observed in V1 (Ji and Wilson, 2006), supporting its involvement. While S1 has been found to engage in motor, but not spatial, memory consolidation (Kumar et al., 2019), to our knowledge, our result is the first evidence showing the involvement of S2 in memory consolidation. Recently spatial selective activity, similar to the place cells in the hippocampus, was found in the S1 and provided a mechanism for location-body coordination (Long and Zhang, 2021). Our network analysis indicated that the S2 was functionally connected to the CA3, warrant further investigation on its interaction with the HPF

in spatial memory formation.

We demonstrate that inhibition of integrator hubs, particularly high-ranking hubs like the LO and LAcbSh, impaired memory formation. Our brain-wide analysis greatly expands a previous study that detected integrator hub in a long-term potentiation evoked network composed of 3 brain regions (Del Ferraro et al., 2018). Although the LO is a critical frontal region for both decision making and the acquisition of hippocampus-dependent memories (Frey and Petrides, 2002; Lesburguères et al., 2011; Vafaei and Rashidy-Pour, 2004), its role in memory consolidation is less understood. Our finding on the LAcbSh is consistent with its involvement in learning and memory (see review (Rinaldi et al., 2012) and integrating spatial information (Ito et al., 2008). Our results support the notion that network integration is a key factor in memory process. This provides another new view of memory consolidation that warrant further investigation. How these integrator hubs are recruited and interact with the HPF and mPFC remain to be elucidated.

In most animal studies, bilateral manipulations are typically used. Whether the same region in both hemispheres has the same function is unclear. Consistent with previous RSN studies (Nasrallah et al., 2016; Tambini and D'Esposito, 2020), we found that post-encoding RSN changes were lateralized. Importantly, we showed that unilateral inhibition was sufficient to impair memory consolidation, consistent with a converging view of functional lateralization of the hippocampus (Jordan, 2020). Alternatively, unilateral inhibition may still affect the contralateral side due to interhemispheric projections. Further study will be needed to clarify this issue.

The hubs identified during the post-learning period could be involved in forming, storing or recalling the memory. We only inhibited the hubs after learning until one day before the probe test. This allowed us to determine their involvement in memory consolidation without affecting memory recall. Whether these hubs are also regions for storing the memory is unclear. This could be further investigated using activity tagging techniques that express DREADDs or channelrhodopsin in active cells after learning and activated them in a different context (ref). Besides, memory consolidation can last for weeks, months or even years (Dudai et al., 2015; Kandel et al., 2014). How these networks transform and interacting with each other over time remain unclear. The changes of RSNs and their hubs at two time points support this ongoing

plasticity. Longitudinal studies with more rsfMRI sessions will provide a broader picture of the trajectory of RSNs during this process. Inhibiting a hub at different time points and conducting rsfMRI scan during hub inhibition would clarify its involvement at a particular time window.

This study has several limitations. First, we only tested a few top-ranking hubs. By comparing with a lower rank hub (S1Tr), we showed that high-ranking hub of network integration is more important. Exhaustively examining all the hubs would be desirable to determine the detection limit of a hub identification criterion. Second, some top-ranking hubs were not tested due to their large volume and lack of subdivision, such as the pons and CPu, in the atlas used. CPu, for instance, is typically not subdivided in structural atlas but shown to be composed of at least 3 functional networks (Zerbi et al., 2015). Further functional subdivision would allow testing specific involvement in memory formation. Third, the rsfMRI was conducted under light sedation. Although this sedative protocol has been shown to be reliable in detecting the RSNs (Grandjean et al., 2014, 2019; Nasrallah et al., 2014) and post-encoding plasticity (Nasrallah et al., 2016; Shah et al., 2018), the detection of certain networks, such as the amygdala, involved in the aversive learning paradigm may be affected (Liang et al., 2014). Awake imaging would allow more comprehensive mapping of functional networks not only post-encoding but also during learning (Han et al., 2019). Finally, which FC contributes to the behavior effect during hub inhibition is unclear. Hub inhibition could affect downstream areas with direct connection and FC with both direct and indirect connections (ref), which may all contribute to the impaired memory. The specificity between FC and behavior could be estimated by correlating behavior with RSNs during hub inhibition and verified by inhibiting each area.

Methods

Animals

100 C57BL/6 male mice (10 - 16 weeks old) were used in the experiments. Animals were housed in transparent cages and maintained on a 12 h light-dark cycle (lights on at 7a.m. and off at 7 p.m.). Food and water were provided *ad libitum*. Experiments were performed during the light phase. All experimental procedures were approved by the animal ethic committee of the University of Queensland and conducted in compliance with the Queensland Animal Care and Protection Act 2001 and the current National Health and Medical Research Council Australian Code of Practice for the Care and Use of Animals for Scientific Purposes.

Experimental design

Two experiments were conducted: one for hub identification (Fig. 1B,C) and the other for hub verification (Fig. 1D). Four groups of mice were used for the hub identification: 1) 1-Day APA (n = 10), 2) 1-Day control (n = 9), 3) 5-Day APA (n = 7), and 4) 5-Day control (n = 5) (see next section for behavior detail). 10 groups were used for hub verification: 3 groups for the common network, 4 groups for network integration, 2 negative controls and one CNO control in naïve mice without surgery.

We utilized DREADDs for targeted inhibition (see surgical section for detail). 4 weeks after the surgery, animals were trained in the 1-Day APA task. Immediately after they finished the last training trial (T5), they were given a water-soluble clozapine *N*-oxide (CNO dihydrochloride; cat #6329, Tocris Bioscience) via intraperitoneal (i.p.) injection (1 mg/kg dissolved in saline), followed by dissolving CNO (1 mg/kg/day) in drinking water to continuously suppress the network hub until one day before the probe test. This one-day interval allows the CNO to be cleared from the body so as minimizing its interference in the probe test (Jendryka et al., 2019). The memory retention in the probe test was used to examine whether the memory consolidation is affected by the hub inhibition.

Behavior

In the APA, an animal stands on a rotating circular arena (Diameter: 0.9 m; rotating speed: 1 rpm) with 4 pictures as spatial cue on each side of the wall (APA equipment: Bio-Signal Group, UAS). Once the animal enters an invisible sector (shock zone) that is stable in relation to a spatial cue, a mild electric shock (0.5mA, 60Hz, 500ms) is administered. The animal needs to

learn to utilize visual cues to identify the exact location of the aversive zone and to avoid it. Two types of training protocols were used:

i. 1-Day APA: animals received five 10-min training sessions with an inter-session interval of ~1 h completed in one day.
ii. 5-Day APA: animals received one 10-min training session each day for 5 consecutive days.

The training starts with habituation (15 min) in which the animal does not receive any shock at one day before the training. Nine days after the last training day, a 10-min probe test was performed to measure the memory retention in the same environment. Foot shock was delivered when the animal enters the aversive zone in the probe test. During each training or probe session, animal behaviors were recorded by a video camera. Two control groups were included: 1-Day sham control and 5-Day sham control. In these groups, animals went through the same APA procedure as the experimental group but did not receive any foot shock. To ensure consistency, all the behavioral experiments were started at the same time of the day.

In behavior data analysis, the number of shocks, the time of first entrance to the shock zone and the maximum time avoidance were analyzed by Bio-Signal Track software (Bio-Signal Group, USA). Repeated measures one-way ANOVA was performed followed by Dunnett test for multiple comparison using Prism (GraphPad Software LLC).

MRI

MRI was conducted on a 9.4 T system (BioSpec 94/30, Bruker BioSpin MRI GmbH, Ettlingen, Germany). Two sessions of rsfMRI scan were performed on each animal in the hub identification. Details of animal preparation, MRI procedure and parameter settings are described in (Lee et al., 2019). Briefly, animals were initially anaesthetized using 3% isoflurane in air and oxygen mixture of a 2:1 ratio. After secured in an MRI-compatible holder using custom tooth and ear bars, a bolus of medetomidine was delivered via an i.p. catheter (0.05-0.1 mg/kg) and the isoflurane level was progressively reduced to 0.25-0.5% over 10 minutes. Then sedative was maintained by a constant i.p. infusion of medetomidine (0.1mg/kg/h) using a syringe pump. Key physiological parameters, including arterial oxygenation saturation (SpO_2), rectal temperature, heart rate and respiratory rate were measured by an MRI-compatible monitoring system (SAII Inc, USA). Internal temperature was maintained at 36.5°C with heated water bath.

After high-order shimming, structural T2-weighted MRI (resolution = 0.1x0.1x0.3 mm^3)

and visual task were conducted first to ensure optimal physiology and neurovascular coupling. Flashing blue light at 5Hz was delivered by an optical fiber in a block design with 21s on and 39s off. Then the rsfMRI was acquired using a multiband gradient-echo echo-planar imaging (Lee et al., 2019) with TR/TE = 300/15 ms, thickness = 0.5 mm, gap = 0.1 mm, 16 axial slices covering the whole cerebrum with in-plane resolution of 0.3 × 0.3 mm^2. 2000 volumes were acquired in 10 min and repeated 3 times with inter-run interval of 2 min. To ensure the consistency, the rsfMRI scan started at ~45min after the bolus injection of medetomidine.

Stereotaxic surgical procedure

Surgeries were performed at least one month before behavior. Animal was anaesthetized by 1.5-2% isoflurane during surgery. Enrofloxacin (6 mg/kg) and carprofen (5 mg/kg) were injected via subcutaneous injections to prevent infection and relieve pain and inflammation respectively. Body temperature was maintained at 37 °C with a heating pad under body. During surgery, 0.25-0.3ul of virus, AAV2/1-pSyn-hM4D(Gi)-T2A-mScarlet, was injected into the target areas based on the coordinates (relative to Bregma) in the Paxions and Franklin Mouse Brain atlas, fifth edition:

(i) $V1_R$. ML: -2.30mm; AP: -4.15mm; DV: -0.50mm.
(ii) $S2_R$. ML: -3.70mm; AP: -0.71mm; DV: -1.40mm.
(iii) $LAcbSh_L$. ML: +1.70mm; AP: +1.10mm; DV: -3.85mm.
(iv) LO_R. ML: -1.65mm; AP: +2.57mm; DV: -1.9mm.
(v) $S1Tr_R$. ML: -1.63mm; AP: -1.60mm; DV: -0.57mm.
(vi) VPM_R. ML: -1.5mm; AP: -1.80mm; DV: -3.3mm.
(vii) FrA_R. ML: -1.70mm; AP: +3.00mm; DV: -0.50mm.

Virus was injected using Nanoject III (Drummond Scientific) with a slow injection rate (0.03 ul/min) over 10 min. The glass pipette stayed for another 6 min and then slowly retracted. After injection, the wound was closed using Vetbond (3M) and suture. Enrofloxacin and carprofen were applied for another two days. Animals were kept in their home cage (group housing of 2-4 animals per cage) for 4 weeks to recover and allow virus to express before starting APA.

Behavior and CNO treatment

The same 1-Day APA task was used for spatial memory training. Right after the 1-Day APA training, water soluble CNO (Tocris Bioscience) was administered to animals via i.p. (1mg/kg,) to inhibit the neuroactivity of the target brain regions. CNO water (1mg/kg/day) was given for

7 days to keep the target brain areas inhibited during memory consolidation. CNO water was replaced with normal water 24 hours before the probe test to minimize the effects of CNO on behavioral performance. On post day 8, a 10 min probe test was performed to test the memory retention.

Histology

Mice were euthanized with an overdose of sodium pentobarbitone and transcardially perfused with 40 ml of PBS, followed by 45 ml of 4% paraformaldehyde in PBS for fixation. The brain was extracted and fixed at 4°C for 12-24 h. It was washed with PBS once and transferred to a 30% sucrose solution for 36 h prior to sectioning. 40 μm thick sections were cut using a sliding microtome and collected in a 1:6 series and one of such series was used for following procedures. Cell nucleus was stained by 4',6-diamidino-2-phenylindole (DAPI, catalog #6329; Sigma Aldrich). Sections were first washed once in PBS for 10 min, and then incubated in 1:5000 DAPI-PBS solution for 15 min at room temperature. After two washes, the sections were mounted on SuperFrost slides using fluorescence mounting medium (Dako, Agilent). Images were captured using a slide scanner (Metafer VSlide Scanner, MetaSystems) and Zeiss Axio Imager Z2 with 20x 0.8 NA / 0.55mm objective lens.

rsfMRI data processing

The rsfMRI data was processed using Matlab (MathWorks Inc, US), FSL (v5.0.11, https://www.fmrib. ox.ac.uk/fsl), AFNI (ver 17.2.05, National Institutes of Health, USA) and ANTs (v2.3.1, http://stnava.github.io/ANTs). The k-space data of the multiband EPI was first phase-corrected and reconstructed in Matlab. After motion correction by FSL mcflirt, the geometric distortion was corrected by FSL TOPUP. The brain mask was extracted automatically using PCNN3D (Chou et al., 2011), followed by manual editing. Nuisance signals including quadratic drift, 6 motion parameters and their derivatives, 10 principal components from tissues outside the brain, and mean signal of the cerebrospinal fluid were then regressed out (Chuang et al., 2019). The data was band-pass filtered at 0.01-0.3 Hz to account for potential frequency shift under sedation. This frequency range could also remove the aliased respiratory and cardiac signal variations in the high sampling rate data. Then the rsfMRI was coregiestered to an EPI template by linear and nonlinear transformations using ANTs. Then the data was smoothed by a 0.6mm Gaussian kernel.

Seed-based correlation analysis was used to measure FC across the brain. Based on the AMBMC atlas (https://imaging.org.au/AMBMC/AMBMC), the brain was divided into 230

bilateral regions of interest (ROIs). The DSURQE atlas (https://wiki.mouseimaging.ca/) was used to label regions not yet defined in the AMBMC, such as the amygdala, hypothalamus, midbrain and brainstem (pons). The mean time-series of each brain region was extracted as a seed signal. Pearson's correlation coefficients between seed time-courses were calculated using AFNI 3dNetCorr. Fisher's z-transformation was used to convert correlation coefficients to z values. Connectivity matrixes from the 3 repeated scans were calculated in each animal. Quality control (QC) was conducted based on the presence of visual task activation. If the visual activation was not detectable, the physiological condition and neurovascular coupling were regarded as sub-optimal, and the scan was discarded. Based on this criterion, 24% of scans were discarded (supplementary Table S2). The matrixes of each animal at each time point that passed the QC were averaged.

Between group difference was calculated by two-sample t-test and thresholded at $p<0.05$ (FDR corrected) using the Network Based Statistics toolbox (https://sites.google.com/site/bctnet/comparison/nbs). For hub identification, a lower threshold (uncorrected) was used to generate a weighted (t-score) network matrix.

Graph theory analysis

To characterize the RSNs, the following graph theory parameters were calculated by the Brain Connectivity Toolbox (http://www.brain-connectivity-toolbox.net) and the graph functions in Matlab:

Global efficacy:

$$E = \frac{1}{n}\sum_{i\in N}\frac{\sum_{j\in N, j\neq i} d_{ij}^{-1}}{n-1}$$

where d_{ij} is the shortest path length between nodes i and j. N is the total number of nodes. A value of 1 indicating maximum efficiency.

Modularity is calculated using the Louvain community detection algorithm:

$$Q = \sum_{u\in M}[e_{uu} - (\sum_{v\in M} e_{uv})^2]$$

where the network is fully subdivided into a set of nonoverlapping modules M, and e_{uv} is the proportion of all links that connect nodes in module u with nodes in module v. The higher Q value, the larger degree of network segregation.

Degree centrality of a node i:

$$k_i = \sum_{j \in N} a_{ij}$$

where a_{ij} is the connection between node i and j: a_{ij} = 1 when link (i, j) exists; a_{ij} = 0 otherwise (a_{ii} = 0 for all i).

Closeness centrality of node i:

$$L_i^{-1} = \frac{n-1}{\sum_{j \in N, j \neq i} d_{ij}}$$

Betweenness centrality of node i:

$$b_i = \frac{1}{(n-1)(n-2)} \sum_{\substack{h,j \in N \\ h \neq j, h \neq i, j \neq i}} \frac{\rho_{hj}(i)}{\rho_{hj}}$$

where ρ_{hj} is the number of shortest paths between nodes h and j, and $\rho_{hj}(i)$ is the number of shortest paths between h and j that pass through i.

Eigenvector centrality of node i :

$$x_i = \frac{1}{\lambda} \sum_{j \in N} a_{ij} x_j$$

where λ is a constant and x is the eigenvector of the binarized network matrix.

Giant component is defined as the largest connected component in a network (Vetere et al., 2017). It can be represented by the number of nodes in the largest connected component. Besides, the ratio of giant component in CI analysis was used to represent the change of giant component when remove node from the network.

FC – behavior correlation

We correlated the strength of each significant FC with two behavior indexes (the number of shocks and the time to first entrance) in the probe test using Pearson correlation coefficient with $p < 0.05$ (two-tailed) regarded as significant. After correlation analysis, we sort the significant connections by their absolute value of correlation coefficient.

Overlap between 1-Day and 5-Day APA

We took out overlapped connections from the network matrix obtained from the two-sample t-test between the APA and control groups ($p < 0.05$, uncorrected). From the overlapped connections, we further did FC – behavior correlation was calculated and sorted (ranked) the significant connections by their absolute value of behavior correlation.

CI analysis

CI analysis was applied to the between-group difference network using an optimized implementation (Zhu, 2018) (https://github.com/zhfkt/ComplexCi/releases). It calculates the value of each node with the following formula:

$$CI_l(i) = (k_i - 1) \sum_{j \in \delta B(i,l)} (k_j - 1)$$

where k_i is the degree of node i, and $\delta B(i, l)$ is the frontier of the ball of radius l which is the set of nodes at distance from i. The value is calculated iteratively by removing nodes until all nodes in the network are eliminated (Morone and Makse, 2015; Morone et al., 2016). In this analysis, we used the ball radius $l = 2$ since we found that larger radius gave nearly the same results. We ranked the nodes according to how fast the size (number of nodes) of "giant component" can collapse by removing the selected node. To find out the reliable ranking list, we calculated the mean CI ranking of each node under three thresholds ($p < 0.05$, $p < 0.01$, $p < 0.005$) and sort the node by the mean CI rank value.

Null distribution of network properties analysis

To examine whether the difference matrixes between APA and control groups are significantly different from random networks, 5000 random networks were created using the function "null_model_und_sign" of the Brain Connectivity Toolbox that preserves the degree and strength distributions of the real network. For each of the 5000 random networks, curves of three network properties, including the giant component, global efficiency and modularity were generated under thresholds ranging from t = 2 to 3.8 (step of 0.2). The AUC of each curve was calculated to form the null distribution for each network property.

Null distribution of common network analysis

To estimate the null distribution of the common network, 5000 permutations of FC matrices were created by randomly assigning individual FC matrix into the APA groups and controls. Between group differences of these permutated matrices were tested by two-sample t-tests and thresholded at $p < 0.05$. The common FC of the permutated 1-Day APA and 5-Day APA data

was correlated with the N_{shock} or T_{enter} of the probe test and thresholded at $p < 0.05$. The number of connections surviving these thresholds from the 5000 permutations formed the null distribution of the common network detection (supplementary Fig. S2A).

Reference

Albert, N.B., Robertson, E.M., and Miall, R.C. (2009). The Resting Human Brain and Motor Learning. Curr. Biol. *19*, 1023–1027.

Bassett, D.S., Wymbs, N.F., Porter, M.A., Mucha, P.J., Carlson, J.M., and Grafton, S.T. (2011). Dynamic reconfiguration of human brain networks during learning. Proc. Natl. Acad. Sci. U. S. A. *108*, 7641–7646.

Bergmann, T.O., and Hartwigsen, G. (2021). Inferring Causality from Noninvasive Brain Stimulation in Cognitive Neuroscience. J. Cogn. Neurosci. *33*, 195–225.

Bielczyk, N.Z., Uithol, S., van Mourik, T., Anderson, P., Glennon, J.C., and Buitelaar, J.K. (2019). Disentangling causal webs in the brain using functional magnetic resonance imaging: A review of current approaches. Netw. Neurosci. *3*, 237–273.

Biswal, B., Yetkin, F.Z., Haughton, V.M., Hyde, J.S., Zerrin Yetkin, F., Haughton, V.M., Hyde, J.S., Yetkin, F.Z., Haughton, V.M., and Hyde, J.S. (1995). Functional connectivity in the motor cortex of resting human brain using echo-planar MRI. Magn. Reson. Med. *34*, 537–541.

Bullmore, E., and Sporns, O. (2009). Complex brain networks: graph theoretical analysis of structural and functional systems. Nat. Rev. Neurosci. *10*, 186–198.

Catani, M., Dell'Acqua, F., and Thiebaut de Schotten, M. (2013). A revised limbic system model for memory, emotion and behaviour. Neurosci. Biobehav. Rev. *37*, 1724–1737.

Chen, T.L., Babiloni, C., Ferretti, A., Perrucci, M.G., Romani, G.L., Rossini, P.M., Tartaro, A., and Del Gratta, C. (2008). Human secondary somatosensory cortex is involved in the processing of somatosensory rare stimuli: An fMRI study. Neuroimage *40*, 1765–1771.

Chou, N., Wu, J., Bai Bingren, J., Qiu, A., and Chuang, K.H. (2011). Robust automatic rodent brain extraction using 3-D pulse-coupled neural networks (PCNN). IEEE Trans. Image Process. *20*, 2554–2564.

Chuang, K.H., and Nasrallah, F.A. (2017). Functional networks and network perturbations in rodents. Neuroimage *163*, 419–436.

Chuang, K.-H., Lee, H.-L., Li, Z., Chang, W.-T., Nasrallah, F.A., Yeow, L.Y., and Singh, K.K.D. /O. R.R. (2019). Evaluation of nuisance removal for functional MRI of rodent brain. Neuroimage *188*, 694–709.

Cimadevilla, J.M., Fenton, A.A., and Bures, J. (2001). New spatial cognition tests for mice: Passive place avoidance on stable and active place avoidance on rotating arenas. Brain Res. Bull. *54*, 559–563.

Cohen, J.R., and D'Esposito, M. (2016). The segregation and integration of distinct brain networks and their relationship to cognition. J. Neurosci. *36*, 12083–12094.
Cole, Cole, D.M., Smith, S.M., and Beckmann, C.F. (2010). Advances and pitfalls in the analysis and interpretation of resting-state FMRI data. Front. Syst. Neurosci. *4*, 1–15.
Craddock, R.C., Jbabdi, S., Yan, C.-G., Vogelstein, J.T., Castellanos, F.X., Di Martino, A., Kelly, C., Heberlein, K., Colcombe, S., and Milham, M.P. (2013). Imaging human connectomes at the macroscale. Nat. Methods *10*, 524–539.
Dablander, F., and Hinne, M. (2019). Node centrality measures are a poor substitute for causal inference. Sci. Reports 2019 91 *9*, 1–13.
Debas, K., Carrier, J., Barakat, M., Marrelec, G., Bellec, P., Tahar, A.H., Karni, A., Ungerleider, L.G., Benali, H., and Doyon, J. (2014). Off-line consolidation of motor sequence learning results in greater integration within a cortico-striatal functional network. Neuroimage *99*, 50–58.
Drew, P.J., Mateo, C., Turner, K.L., Yu, X., and Kleinfeld, D. (2020). Ultra-slow Oscillations in fMRI and Resting-State Connectivity: Neuronal and Vascular Contributions and Technical Confounds. Neuron *107*, 782–804.
Drysdale, A.T., Grosenick, L., Downar, J., Dunlop, K., Mansouri, F., Meng, Y., Fetcho, R.N., Zebley, B., Oathes, D.J., Etkin, A., et al. (2016). Resting-state connectivity biomarkers define neurophysiological subtypes of depression. Nat. Med. 2016 231 *23*, 28–38.
Dudai, Y., Karni, A., and Born, J. (2015). The Consolidation and Transformation of Memory. Neuron *88*, 20–32.
Duncan, N.W., and Northoff, G. (2013). Overview of potential procedural and participant-related confounds for neuroimaging of the resting state. J. Psychiatry Neurosci. *38*, 84.
Eichenbaum, H. (2017). Prefrontal–hippocampal interactions in episodic memory. Nat. Rev. Neurosci. 2017 189 *18*, 547–558.
Etkin, A., Egner, T., and Kalisch, R. (2011). Emotional processing in anterior cingulate and medial prefrontal cortex. Trends Cogn. Sci. *15*, 85–93.
Del Ferraro, G., Moreno, A., Min, B., Morone, F., Pérez-Ramírez, Ú., Pérez-Cervera, L., Parra, L.C., Holodny, A., Canals, S., and Makse, H.A. (2018). Finding influential nodes for integration in brain networks using optimal percolation theory. Nat. Commun. *9*.
Fornito, A., Zalesky, A., and Breakspear, M. (2015). The connectomics of brain disorders. Nat. Rev. Neurosci. 2015 163 *16*, 159–172.
Fox, M.D., Halko, M.A., Eldaief, M.C., and Pascual-Leone, A. (2012). Measuring and manipulating brain connectivity with resting state functional connectivity magnetic resonance

imaging (fcMRI) and transcranial magnetic stimulation (TMS). Neuroimage *62*, 2232–2243.
Frey, S., and Petrides, M. (2002). Orbitofrontal cortex and memory formation. Neuron *36*, 171–176.
Gonzalez-Castillo, J., Kam, J.W.Y., Hoy, C.W., and Bandettini, P.A. (2021). How to Interpret Resting-State fMRI: Ask Your Participants. J. Neurosci. *41*, 1130–1141.
Goode, T.D., Ressler, R.L., Acca, G.M., Miles, O.W., and Maren, S. (2019). Bed nucleus of the stria terminalis regulates fear to unpredictable threat signals. Elife *8*.
Goode, T.D., Tanaka, K.Z., Sahay, A., and McHugh, T.J. (2020). An Integrated Index: Engrams, Place Cells, and Hippocampal Memory. Neuron *107*, 805–820.
Grandjean, J., Schroeter, A., Batata, I., and Rudin, M. (2014). Optimization of anesthesia protocol for resting-state fMRI in mice based on differential effects of anesthetics on functional connectivity patterns. Neuroimage *102*, 838–847.
Grandjean, J., Canella, C., Anckaerts, C., Ayrancı, G., Bougacha, S., Bienert, T., Buehlmann, D., Coletta, L., Gallino, D., Gass, N., et al. (2019). Common functional networks in the mouse brain revealed by multi-centre resting-state fMRI analysis. BioRxiv 541060.
Greicius, M.D., Krasnow, B., Reiss, A.L., and Menon, V. (2003). Functional connectivity in the resting brain: A network analysis of the default mode hypothesis. Proc. Natl. Acad. Sci. *100*, 253–258.
Han, Z., Chen, W., Chen, X., Zhang, K., Tong, C., Zhang, X., Li, C.T., and Liang, Z. (2019). Awake and behaving mouse fMRI during Go/No-Go task. Neuroimage *188*, 733–742.
Headley, D.B., and Paré, D. (2017). Common oscillatory mechanisms across multiple memory systems. Npj Sci. Learn. *2*, 1.
Hernandez, P.J., Sadeghian, K., and Kelley, A.E. (2002). Early consolidation of instrumental learning requires protein synthesis in the nucleus accumbens. Nat. Neurosci. 2002 512 *5*, 1327–1331.
van den Heuvel, M.P., and Sporns, O. (2019). A cross-disorder connectome landscape of brain dysconnectivity. Nat. Rev. Neurosci. 2019 207 *20*, 435–446.
Ito, R., Robbins, T.W., Pennartz, C.M., and Everitt, B.J. (2008). Functional interaction between the hippocampus and nucleus accumbens shell is necessary for the acquisition of appetitive spatial context conditioning. J. Neurosci. *28*, 6950–6959.
Jendryka, M., Palchaudhuri, M., Ursu, D., van der Veen, B., Liss, B., Kätzel, D., Nissen, W., and Pekcec, A. (2019). Pharmacokinetic and pharmacodynamic actions of clozapine-N-oxide, clozapine, and compound 21 in DREADD-based chemogenetics in mice. Sci. Reports 2019 91 *9*, 1–14.

Ji, D., and Wilson, M.A. (2006). Coordinated memory replay in the visual cortex and hippocampus during sleep. Nat. Neurosci. 2007 101 *10*, 100–107.
Jordan, J.T. (2020). The rodent hippocampus as a bilateral structure: A review of hemispheric lateralization. Hippocampus *30*, 278–292.
Kandel, E.R., Dudai, Y., and Mayford, M.R. (2014). The molecular and systems biology of memory. Cell *157*, 163–186.
Kao, C.H., Khambhati, A.N., Bassett, D.S., Nassar, M.R., McGuire, J.T., Gold, J.I., and Kable, J.W. (2020). Functional brain network reconfiguration during learning in a dynamic environment. Nat. Commun. *11*, 1–13.
Keerativittayayut, R., Aoki, R., Sarabi, M.T., Jimura, K., and Nakahara, K. (2018). Large-scale network integration in the human brain tracks temporal fluctuations in memory encoding performance. Elife *7*, e32696.
Kim, K., Ekstrom, A.D., and Tandon, N. (2016). A network approach for modulating memory processes via direct and indirect brain stimulation: Toward a causal approach for the neural basis of memory. Neurobiol. Learn. Mem. *134*, 162–177.
Kitamura, T., Ogawa, S.K., Roy, D.S., Okuyama, T., Morrissey, M.D., Smith, L.M., Redondo, R.L., and Tonegawa, S. (2017). Engrams and circuits crucial for systems consolidation of a memory. Science (80-.). *356*, 73–78.
Kumar, N., Manning, T.F., and Ostry, D.J. (2019). Somatosensory cortex participates in the consolidation of human motor memory. PLOS Biol. *17*, e3000469.
Lee, H.L., Li, Z., Coulson, E.J., and Chuang, K.H. (2019). Ultrafast fMRI of the rodent brain using simultaneous multi-slice EPI. Neuroimage *195*, 48–58.
Lesburguères, E., Gobbo, O.L., Alaux-Cantin, S., Hambucken, A., Trifilieff, P., and Bontempi, B. (2011). Early tagging of cortical networks is required for the formation of enduring associative memory. Science (80-.). *331*, 924–928.
Lesburguères, E., Sparks, F.T., O'Reilly, K.C., and Fenton, A.A. (2016). Active place avoidance is no more stressful than unreinforced exploration of a familiar environment. Hippocampus *26*, 1481–1485.
Liang, Z., King, J., and Zhang, N. (2014). Neuroplasticity to a single-episode traumatic stress revealed by resting-state fMRI in awake rats. Neuroimage *103*, 485–491.
Liu, J., Xia, M., Dai, Z., Wang, X., Liao, X., Bi, Y., and He, Y. (2016). Intrinsic Brain Hub Connectivity Underlies Individual Differences in Spatial Working Memory. Cereb. Cortex *27*, 5496–5508.
Liu, X., Ramirez, S., Pang, P.T., Puryear, C.B., Govindarajan, A., Deisseroth, K., and

Tonegawa, S. (2012). Optogenetic stimulation of a hippocampal engram activates fear memory recall. Nature *484*, 381–385.
Long, X., and Zhang, S.-J. (2021). A novel somatosensory spatial navigation system outside the hippocampal formation. Cell Res. 1–15.
Managò, F., Castellano, C., Oliverio, A., Mele, A., and De Leonibus, E. (2009). Role of dopamine receptors subtypes, D1-like and D2-like, within the nucleus accumbens subregions, core and shell, on memory consolidation in the one-trial inhibitory avoidance task. Learn. Mem. *16*, 46–52.
Matthews, P.M., and Hampshire, A. (2016). Clinical Concepts Emerging from fMRI Functional Connectomics. Neuron *91*, 511–528.
Mele, A., Avena, M., Roullet, P., De Leonibus, E., Mandillo, S., Sargolini, F., Coccurello, R., and Oliverio, A. (2004). Nucleus accumbens dopamine receptors in the consolidation of spatial memory. Behav. Pharmacol. *15*, 423–431.
Metcalfe, J., Funnell, M., and Gazzaniga, M.S. (2016). Right-Hemisphere Memory Superiority: Studies of a Split-Brain Patient: Https://Doi.Org/10.1111/j.1467-9280.1995.Tb00325.X *6*, 157–164.
Milczarek, M.M., and Vann, S.D. (2020). The retrosplenial cortex and long-term spatial memory: from the cell to the network. Curr. Opin. Behav. Sci. *32*, 50–56.
Milczarek, M.M., Vann, S.D., Sengpiel, F., Milczarek, M.M., Vann, S.D., and Sengpiel, F. (2018). Spatial Memory Engram in the Mouse Retrosplenial Cortex. Curr. Biol. *28*, 1975-1980.e6.
Mill, R.D., Ito, T., and Cole, M.W. (2017). From connectome to cognition: The search for mechanism in human functional brain networks. Neuroimage *160*, 124–139.
Miller, J., Watrous, A.J., Tsitsiklis, M., Lee, S.A., Sheth, S.A., Schevon, C.A., Smith, E.H., Sperling, M.R., Sharan, A., Asadi-Pooya, A.A., et al. (2018). Lateralized hippocampal oscillations underlie distinct aspects of human spatial memory and navigation. Nat. Commun. *9*, 1–12.
Morone, F., and Makse, H.A. (2015). Influence maximization in complex networks through optimal percolation. Nature *524*, 65–68.
Morone, F., Min, B., Bo, L., Mari, R., and Makse, H.A. (2016). Collective Influence Algorithm to find influencers via optimal percolation in massively large social media. Sci. Rep. *6*, 1–11.
Nasrallah, F.A., Tay, H.C., and Chuang, K.H. (2014). Detection of functional connectivity in the resting mouse brain. Neuroimage *86*, 417–424.

Nasrallah, F.A., To, X.V., Chen, D.Y., Routtenberg, A., and Chuang, K.H. (2016). Functional connectivity MRI tracks memory networks after maze learning in rodents. Neuroimage *127*, 196–202.

Paul, C.M., Magda, G., and Abel, S. (2009). Spatial memory: Theoretical basis and comparative review on experimental methods in rodents. Behav. Brain Res. *203*, 151–164.

Phelps, E.A., and Hofmann, S.G. (2019). Memory editing from science fiction to clinical practice. Nature *572*, 43–50.

Pievani, M., Filippini, N., van den Heuvel, M.P., Cappa, S.F., and Frisoni, G.B. (2014). Brain connectivity in neurodegenerative diseases—from phenotype to proteinopathy. Nat. Rev. Neurol. *10*, 620–633.

Ranganath, C., and Ritchey, M. (2012). Two cortical systems for memory-guided behaviour. Nat. Rev. Neurosci. 2012 1310 *13*, 713–726.

Raper, J., Morrison, R.D., Daniels, J.S., Howell, L., Bachevalier, J., Wichmann, T., and Galvan, A. (2017). Metabolism and Distribution of Clozapine-N-oxide: Implications for Nonhuman Primate Chemogenetics. ACS Chem. Neurosci. *8*, 1570–1576.

Reid, A.T., Headley, D.B., Mill, R.D., Sanchez-Romero, R., Uddin, L.Q., Marinazzo, D., Lurie, D.J., Valdés-Sosa, P.A., Hanson, S.J., Biswal, B.B., et al. (2019). Advancing functional connectivity research from association to causation. Nat. Neurosci. *22*, 1751–1760.

Rinaldi, A., Oliverio, A., and Mele, A. (2012). Spatial memory, plasticity and nucleus accumbens. Rev. Neurosci. *23*, 527–541.

Rolls, E.T. (2015). Limbic systems for emotion and for memory, but no single limbic system. Cortex *62*, 119–157.

Sandrini, M., Cohen, L.G., and Censor, N. (2015). Modulating reconsolidation: a link to causal systems-level dynamics of human memories. Trends Cogn. Sci. *19*, 475–482.

Shah, D., Verhoye, M., Van der Linden, A., and D'Hooge, R. (2018). Acquisition of Spatial Search Strategies and Reversal Learning in the Morris Water Maze Depend on Disparate Brain Functional Connectivity in Mice. Cereb. Cortex 1–11.

Shinohara, Y., Hosoya, A., Yamasaki, N., Ahmed, H., Hattori, S., Eguchi, M., Yamaguchi, S., Miyakawa, T., Hirase, H., and Shigemoto, R. (2012). Right-hemispheric dominance of spatial memory in split-brain mice. Hippocampus *22*, 117–121.

Sousa, A.F. De, Cowansage, K.K., Zutshi, I., Cardozo, L.M., Yoo, E.J., Leutgeb, S., De Sousa, A.F., Cowansage, K.K., Zutshi, I., Cardozo, L.M., et al. (2019). Optogenetic reactivation of memory ensembles in the retrosplenial cortex induces systems consolidation. Proc. Natl. Acad. Sci. U. S. A. *116*, 8576–8581.

Tambini, A., and D'Esposito, M. (2020). Causal Contribution of Awake Post-encoding Processes to Episodic Memory Consolidation. Curr. Biol. *30*, 3533-3543.e7.
Tambini, A., Ketz, N., and Davachi, L. (2010). Enhanced Brain Correlations during Rest Are Related to Memory for Recent Experiences. Neuron *65*, 280–290.
Tucker, D.M., Hartry-Speiser, A., McDougal, L., Luu, P., and Degrandpre, D. (1999). Mood and spatial memory: emotion and right hemisphere contribution to spatial cognition. Biol. Psychol. *50*, 103–125.
Ullmann, J.F.P., Watson, C., Janke, A.L., Kurniawan, N.D., and Reutens, D.C. (2013). A segmentation protocol and MRI atlas of the C57BL/6J mouse neocortex. Neuroimage *78*, 196–203.
Vafaei, A.A., and Rashidy-Pour, A. (2004). Reversible lesion of the rat's orbitofrontal cortex interferes with hippocampus-dependent spatial memory. Behav. Brain Res. *149*, 61–68.
van de Ven, V., Jacobs, C., and Sack, A.T. (2012). Topographic Contribution of Early Visual Cortex to Short-Term Memory Consolidation: A Transcranial Magnetic Stimulation Study. J. Neurosci. *32*, 4–11.
Vetere, G., Kenney, J.W., Tran, L.M., Xia, F., Steadman, P.E., Parkinson, J., Josselyn, S.A., and Frankland, P.W. (2017). Chemogenetic Interrogation of a Brain-wide Fear Memory Network in Mice. Neuron *94*, 363-374.e4.
Wang, J.X., Rogers, L.M., Gross, E.Z., Ryals, A.J., Dokucu, M.E., Brandstatt, K.L., Hermiller, M.S., and Voss, J.L. (2014). Targeted enhancement of cortical-hippocampal brain networks and associative memory. Science (80-.). *345*, 1054–1057.
Yu, M., Sporns, O., and Saykin, A.J. (2021). The human connectome in Alzheimer disease — relationship to biomarkers and genetics. Nat. Rev. Neurol. 2021 179 *17*, 545–563.
Zerbi, V., Grandjean, J., Rudin, M., and Wenderoth, N. (2015). Mapping the mouse brain with rs-fMRI: An optimized pipeline for functional network identification. Neuroimage *123*, 11–21.
Zhang, D., Wang, J., Liu, X., Chen, J., and Liu, B. (2015). Aberrant brain network efficiency in Parkinson's disease patients with tremor: A multi-modality study. Front. Aging Neurosci. *7*, 31.
Zhu, F. (2018). Improved collective influence of finding most influential nodes based on disjoint-set reinsertion. Sci. Rep. *8*, 1–12.

Author contribution

K.C., P.O. and P.S. contributed to designing experiments.

Z.L., D.A. and K.C. conducted experiments and data analysis.

ZL, KC and xx wrote the manuscript.

Acknowledgement

This study was funded by the Australian Research Council Discovery Project grant #180103319. Z.L. was supported by Research Training Program scholarship of the University of Queensland.

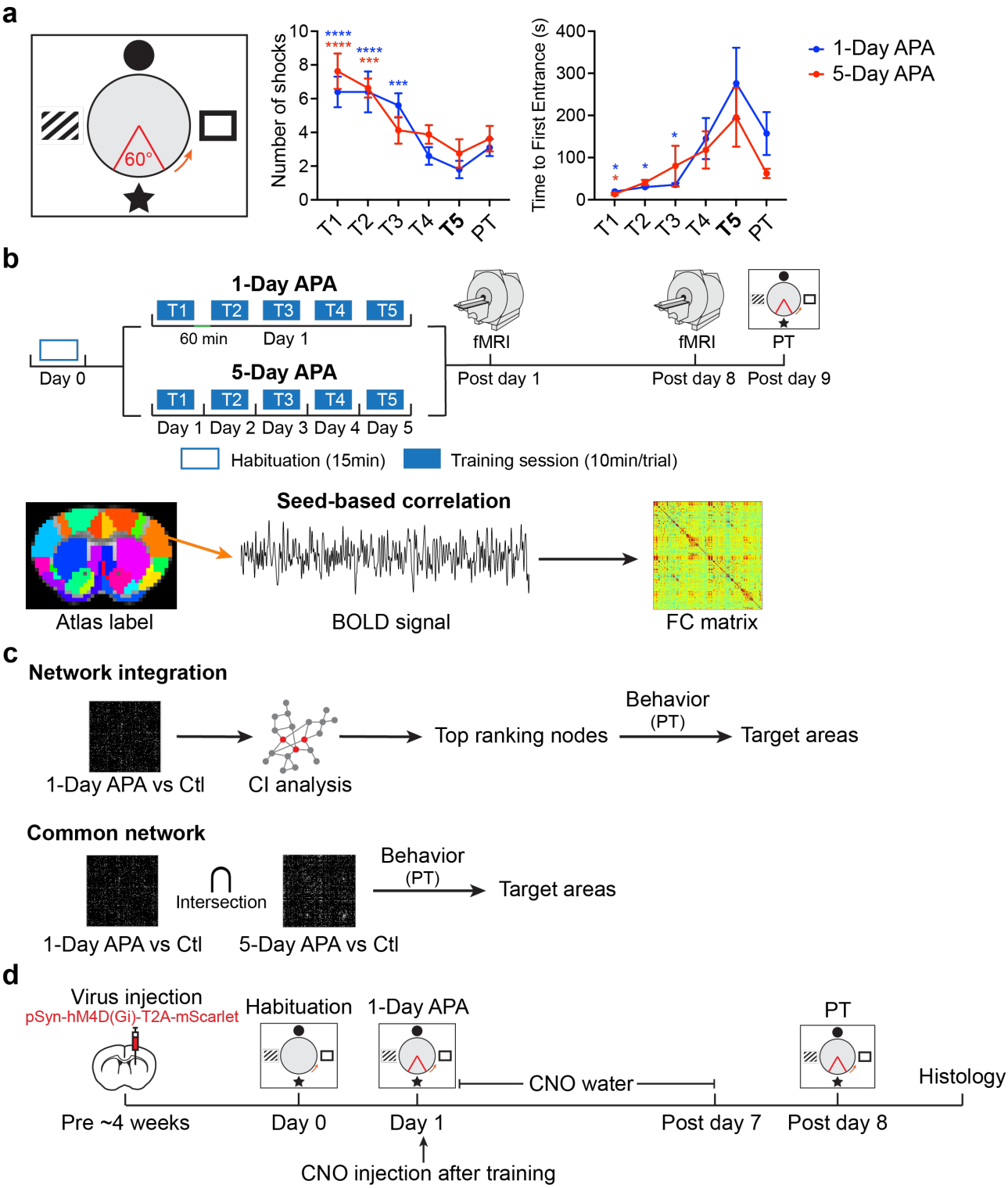

Figure 1 Experimental design & behavior

(A) The left diagram shows the setup of the APA task. Four distinct pictures were hung on the surrounding walls as visual cues. The orange arrow indicates the rotating direction. The red sector shows the location of the invisible "shock zone". The right two plots show the curves of the number of shocks and the time to first entrance in 1-Day and 5-Day APA. Comparisons are performed between the last training trial (T5) and other training trials (T1 to T4) or probe test (PT). Data are represented as mean ± SEM. * $p < 0.05$; *** $p < 0.001$; **** $p<0.0001$. (B) The schematic diagram of the APA-rsfMRI experiment and the procedure of seed-based correlation for creating the FC matrix of each animal. (C) Procedures of identifying key hubs based on network integration and common network. The difference FC matrix between the APA and control (Ctl) groups were

calculated by two-sample t-test. (D) The schematic diagram of target validation using DREADDs inhibition.

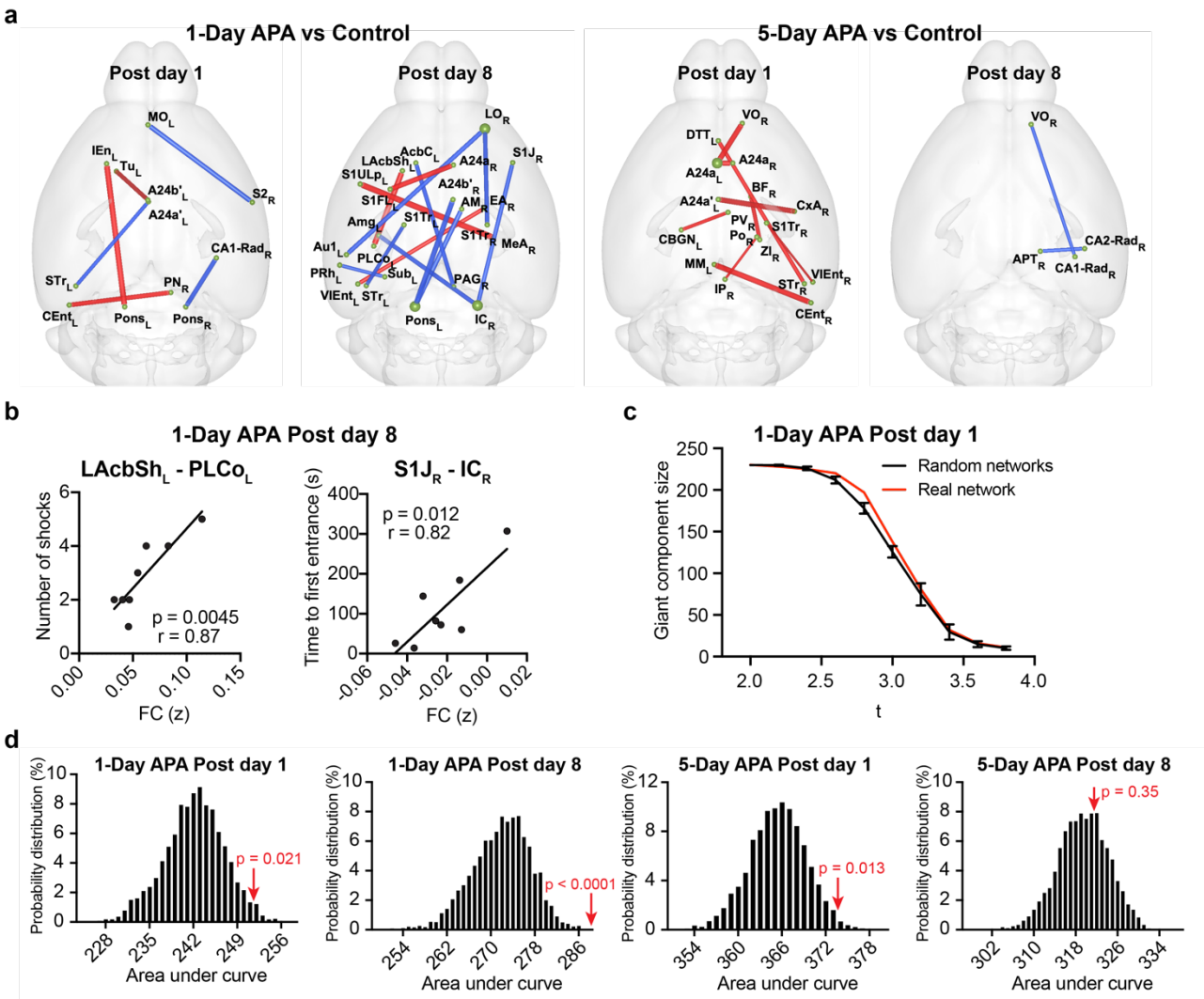

Figure 2 Dynamics and characteristics of post-encoding RSNs

(A) Changed functional connections in 1-Day and 5-Day APA on post day 1 and post day 8 ($p < 0.05$, FDR corrected). The node size indicates the degree of the node. The red connections are APA > control while the blue ones are APA < control. The line thickness indicates the t value. (B) Two functional connections from 1-Day APA post day 8 correlated with the behaviors of memory retention probe test. (C) Example trends of giant component size from 1-Day APA post day 1 (red) compared to random networks (black), thresholded at $2 \leq t \leq 3.8$. The black line shows the mean ± SD of 5000 random networks generated based on the real network. (D) Null distribution of the area under curve as shown in (C). The red arrows indicate the value of real network and the corresponding p value.

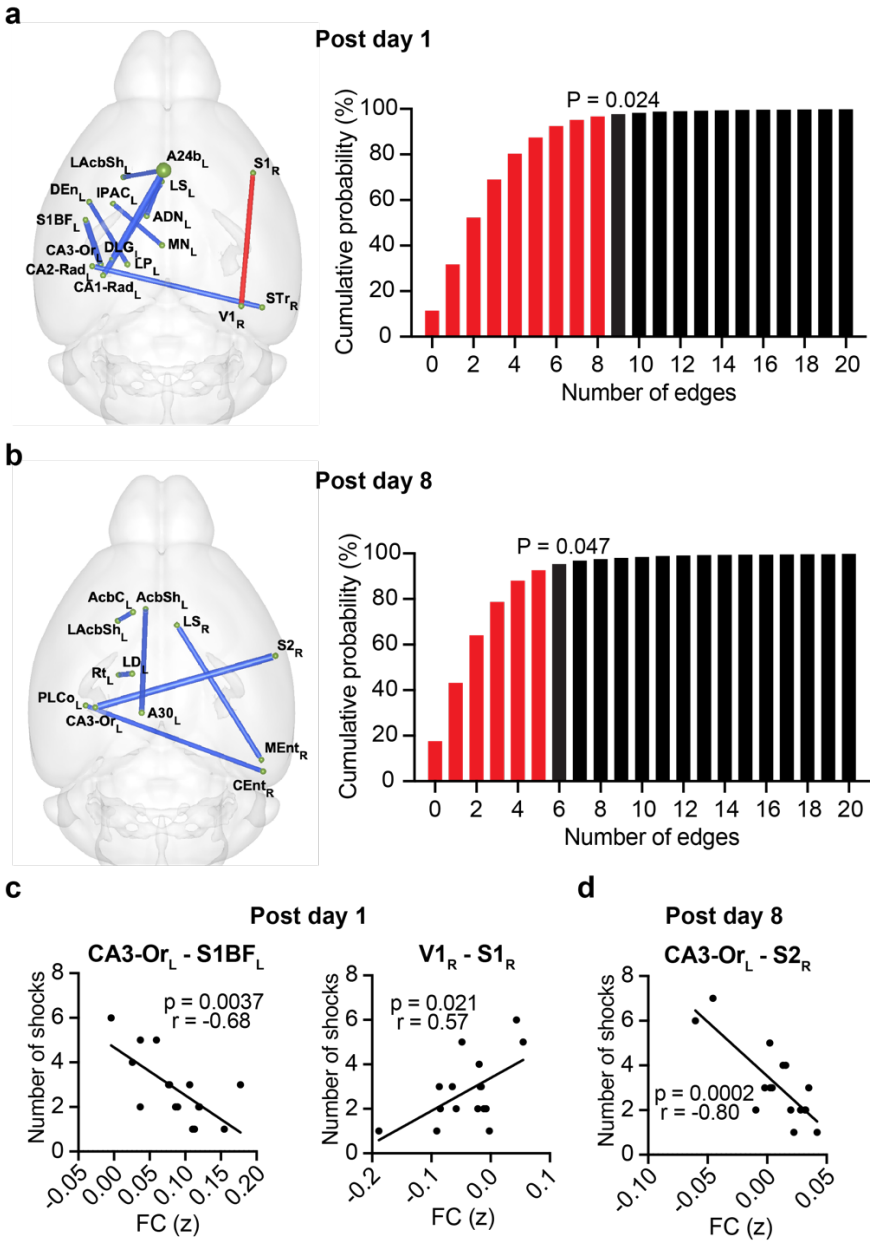

Figure 3 Identification of common networks

(A) The image shows functional connections correlated with N_{shock} ($p<0.05$) within the common networks of 1-Day and 5-Day APA on post day 1. The node size indicates the degree of the node. The red lines show the functional connections positively correlated with N_{shock} while the blue lines show the ones negatively correlated with N_{shock}. The line width indicates the absolute r value. On the right shows the cumulative distribution of the 5000 permutation tests. The red bars represent the cumulative probability before reaching to the real number of edges (9 connections). (B) The common behavior correlated connections on post day 8 and the corresponding cumulative distribution of the 5000 permutation tests. (C) Behavior correlation plots of the functional connections with the target hubs from post day 1 or post day 8 dataset.

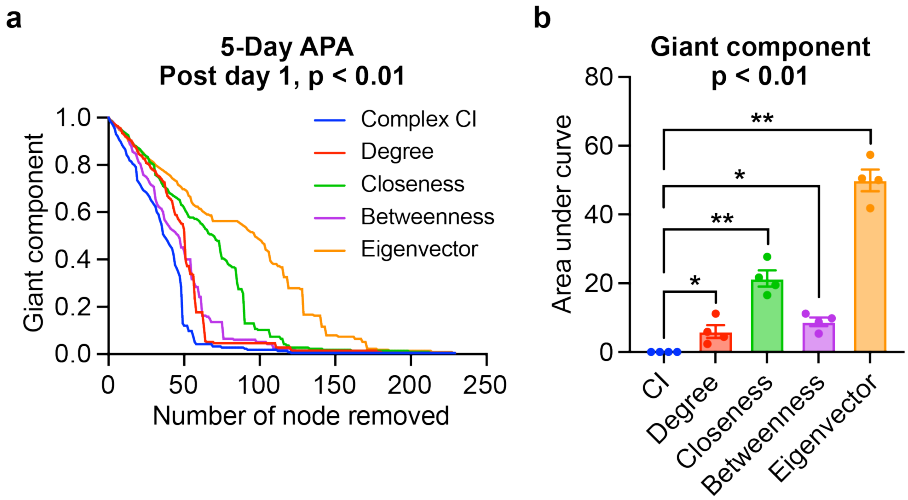

Figure 4 Comparison of hub selection methods based on network integration.
(A) Trends of reduction in giant component from 5-Day APA, post day 1. Five hub selection methods include CI, degree centrality, closeness centrality, betweenness centrality, and eigenvector centrality. Each line represents the proportion of remaining giant component after the nodes are removed from the network one by one according to the rank obtained using each mothed. The quicker the giant component drops, the faster the original network breaks into smaller networks (reduced integration). (B) The AUC of the giant component reduction curves when the networks were thresholded at $p<0.01$ uncorrected. It includes datasets of 1-Day APA and 5-Day APA on both post day 1 and post day 8 when comparing APA and control groups. Each data point was normalized by the corresponding AUC of CI. One-way ANOVA, $F = 50.36$, $p < 0.0001$. Data are represented as mean ± SEM. * $p < 0.05$; ** $p < 0.01$.

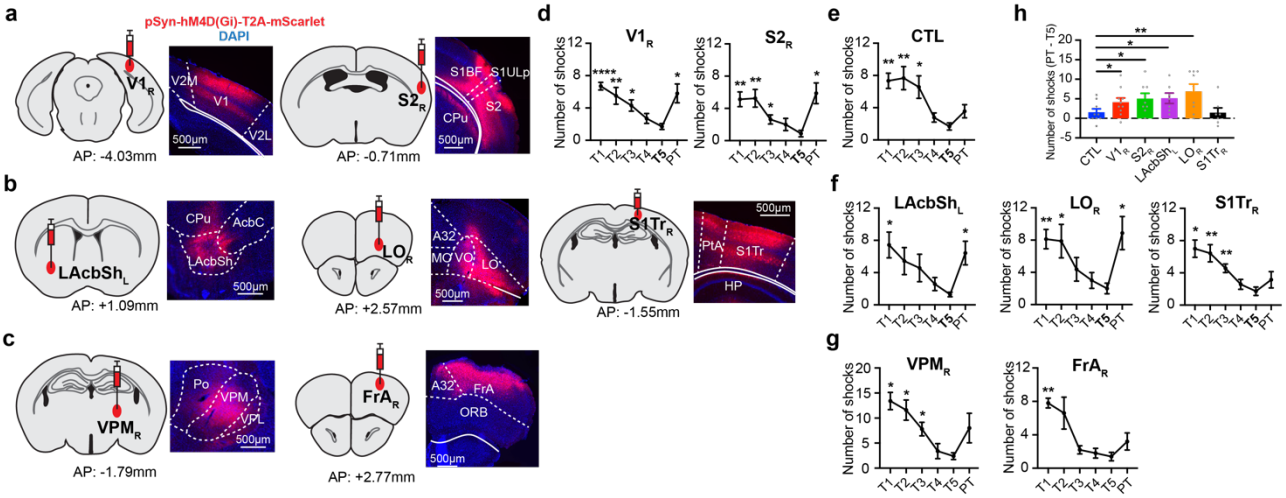

Figure 5 DREADDs expression and behaviour effects of hub inhibition

Representative AAV expression in the target areas selected from (A) common networks (B) network integration and (C) negative control. In each subgraph, the left image shows the injecting location of AAV-pSyn-hM4D(Gi)-T2A-mScarlet, and the right image shows the fluorescence imaging. (D-G) show the number of shock during 1-Day APA learning (T1 to T5) and probe test (PT) after DREADDs inhibition during the consolidation period and in the CNO-control (CTL). All the comparisons are performed between the last training trial (T5) and other training trials or probe tests. (H) Comparison of changed number of shocks (PT – T5) between experimental groups and CNO-control group. One-way ANOVA, $F = 2.58$, $p = 0.04$. Data are represented as mean ± SEM. * $p < 0.05$; ** $p < 0.01$; **** $p<0.0001$. A32, Prelimbic area; AcbC, accumbens nucleus, core region; CPu, caudate putamen; FrA, frontal association cortex; HP, hippocampus; LAcbSh, lateral accumbens, shell region; LO, lateral orbital cortex; MO, medial orbital cortex; ORB, orbital cortex; Po, posterior thalamic nuclear group; PtA, parietal association cortex; S1BF, primary somatosensory cortex, barrel field; S1Tr, primary somatosensory, trunk; S1ULP, primary somatosensory cortex, upper lip; S2, secondary somatosensory cortex; V1: primary visual cortex; V2L, secondary visual cortex, lateral; V2M, secondary visual cortex, medial; VO, ventral orbital cortex; VPL, ventral posterolateral thalamic nucleus; VPM, ventral posteromedial thalamic nucleus.

Table 1 Top 10 nodes for network integration identified by CI analysis.
This table shows the top 10 ranking nodes according to the mean CI rank under network threshold of $p < 0.05$, $p < 0.01$ and $p < 0.005$ when comparing 1-Day APA and control. $_R$: right hemisphere; $_L$: left hemisphere.

Post day 1		Post day 8	
Node	**Mean CI Rank**	**Node**	**Mean CI Rank**
$Pons_R$	1.0	$MPtA_R$	6.7
$LAcbSh_L$	3.7	PAG_R	7.0
$VIEnt_L$	9.3	LO_R	7.3
PN_R	9.7	VM_L	10.7
MB_R	10.0	$S1FL_L$	12.0
CPu_R	13.0	Hyp_L	14.3
MM_R	13.7	LD_R	15.3
STr_L	15.3	LS_R	17.0
$CEnt_L$	21.7	$LAcbSh_R$	20.0
$S2_L$	22.0	$S1Tr_R$	21.7

Table 2 Behavior correlated functional connections containing the top 10 CI nodes.
Each row shows the names of the nodes, the behavioral correlation r and p values. Brain regions shown in **bold** are the top 10 ranking nodes in CI analysis (shown in Table 1). $_R$: right hemisphere; $_L$: left hemisphere.

		Node 1	Structure name 1	Node 2	Structure name 2	r	p value
Post day 1	$\mathbf{N_{shock}}$	CA1-Lmol$_R$	CA1-Lmol	**CPu$_R$**	Caudate putamen	-0.79	0.0063
		CEnt$_L$	Caudomedial entorhinal cortex	GP$_R$	Globus pallidus	-0.78	0.0081
		LH$_L$	Lateral hypothalamus	**PN$_R$**	Pontine nucleus	-0.72	0.018
		Tu$_L$	Olfactory tubercle	**VIEnt$_L$**	Ventral intermediate entorhinal cortex	-0.69	0.029
	$\mathbf{T_{enter}}$	**LAcbSh$_L$**	Accumbens nucleus shell, lateral part	Rt$_R$	Reticular nucleus (prethalamus)	0.95	3.70E-05
		Tu$_L$	Olfactory tubercle	**VIEnt$_L$**	Ventral intermediate entorhinal cortex	0.82	0.0035
		CEnt$_L$	Caudomedial entorhinal cortex	GP$_R$	Globus pallidus	0.82	0.004
Post day 8	$\mathbf{N_{shock}}$	**VM$_L$**	Ventromedial thalamic nucleus	A30$_L$	Retrosplenial area, dorsal part	0.91	0.0015
		S1FL$_L$	Primary somatosensory cortex, forelimb region	MeA$_R$	Medial amygdala	0.89	0.0033
		VL$_L$	Ventrolateral thalamic nucleus	**LO$_R$**	Lateral orbial cortex	0.87	0.0045
		EA$_L$	Extension of the amygdala	**PAG$_R$**	Periaqueductal gray	-0.84	0.0088
		PoDG$_R$	Dentate-Gyrus-PoDG	**S1Tr$_R$**	Primary somatosensory cortex, trunk region	-0.84	0.0095
		VO$_L$	Ventral orbital cortex	**S1Tr$_R$**	Primary somatosensory cortex, trunk region	0.79	0.02
		Hyp$_L$	Hypothalamus	DTT$_R$	Dorsal tenia tecta	0.75	0.031
	$\mathbf{T_{enter}}$	**S1FL$_L$**	Primary somatosensory cortex, forelimb region	MeA$_R$	Medial amygdala	-0.8	0.018

Supplementary Data

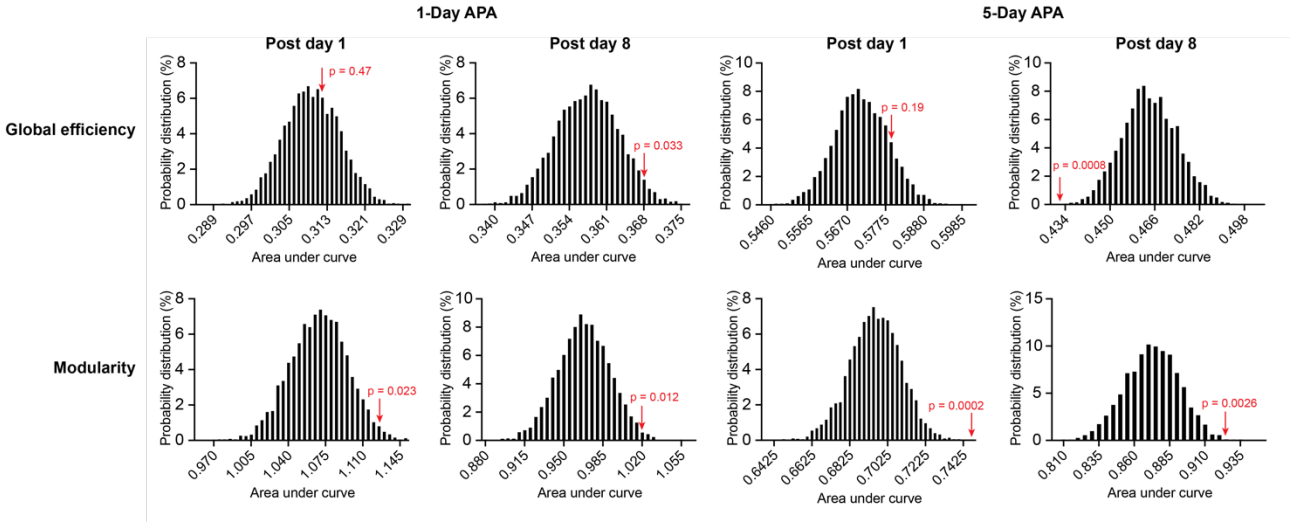

Figure S1 Null distribution of APA training on network properties.
Probability distribution of the area under curves of global efficiency and modularity of 5000 random networks. The red arrows indicate the location of real results.

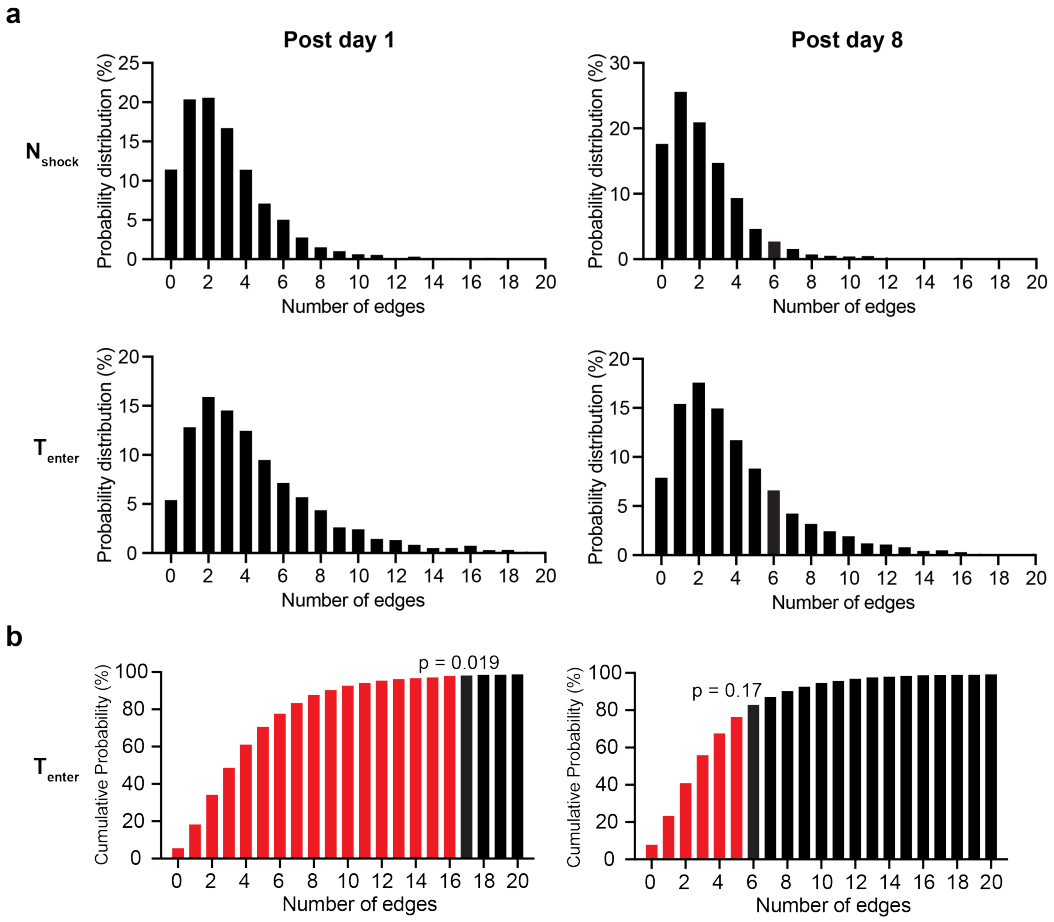

Figure S2 Null distribution of permutation test of the common network.
(A) The null distribution of the number of edges when 5000 permutated networks of 1-Day and 5-Day APA were thresholded at $p<0.05$ and correlated with N_{shock} or T_{enter} at $p<0.05$. (B) The cumulative probability of the null distribution in (A) when correlated with the T_{enter}. The red bars show the cumulative probability before reaching to the real number of edges.

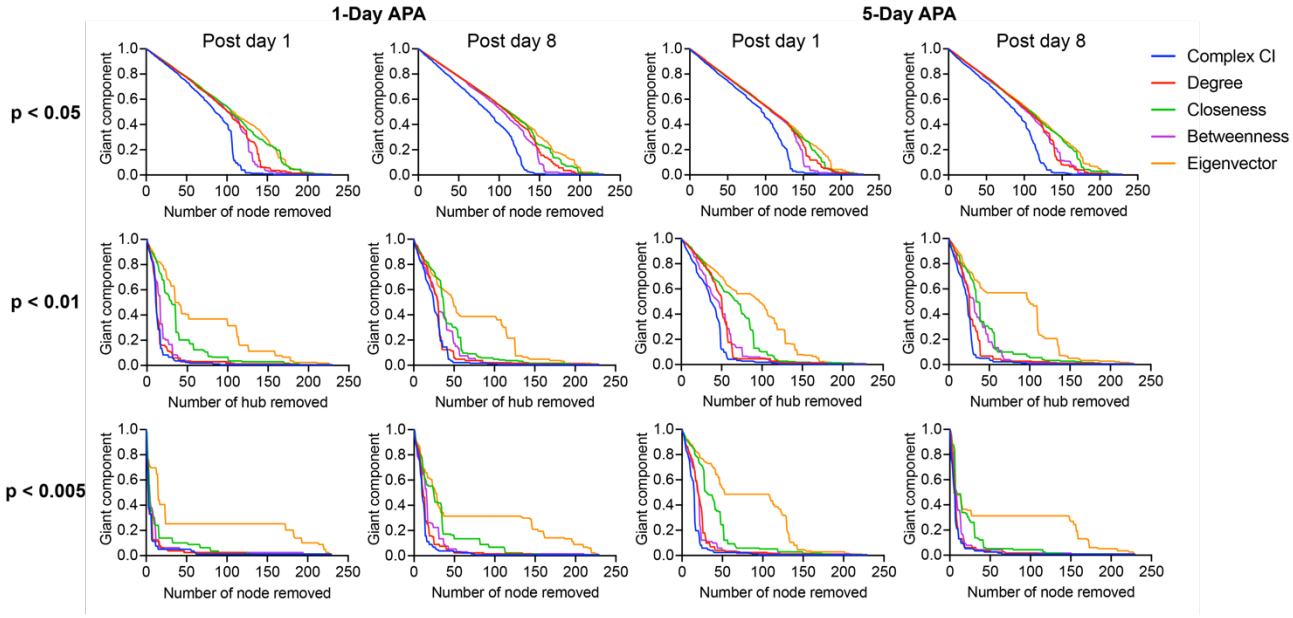

Figure S3 Giant component reduction by removing integrator hubs under different network thresholds.

Five hub selection methods were compared, including CI, degree centrality, closeness centrality, betweenness centrality, and eigenvector centrality. Each line represents the remaining proportion of giant component after the nodes are removed from the network one by one according to the rank obtained using each mothed.

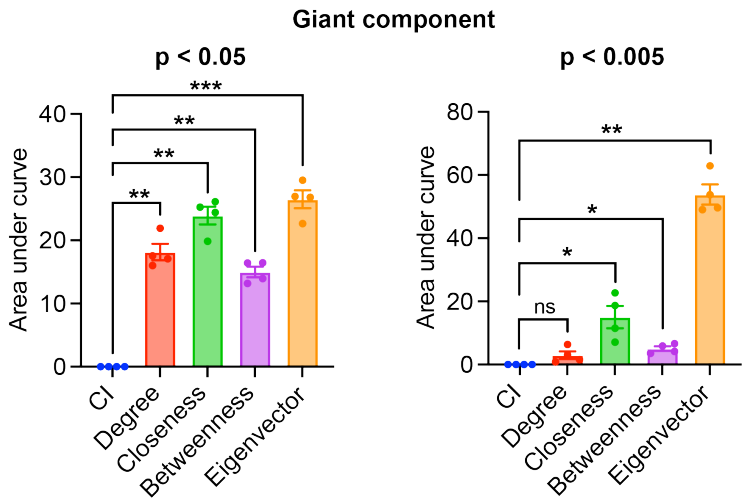

Figure S4 Comparison of efficiency in reducing giant component.
CI analysis shows the quickest reduction of giant components when the network was thresholded at p<0.05 or 0.005.

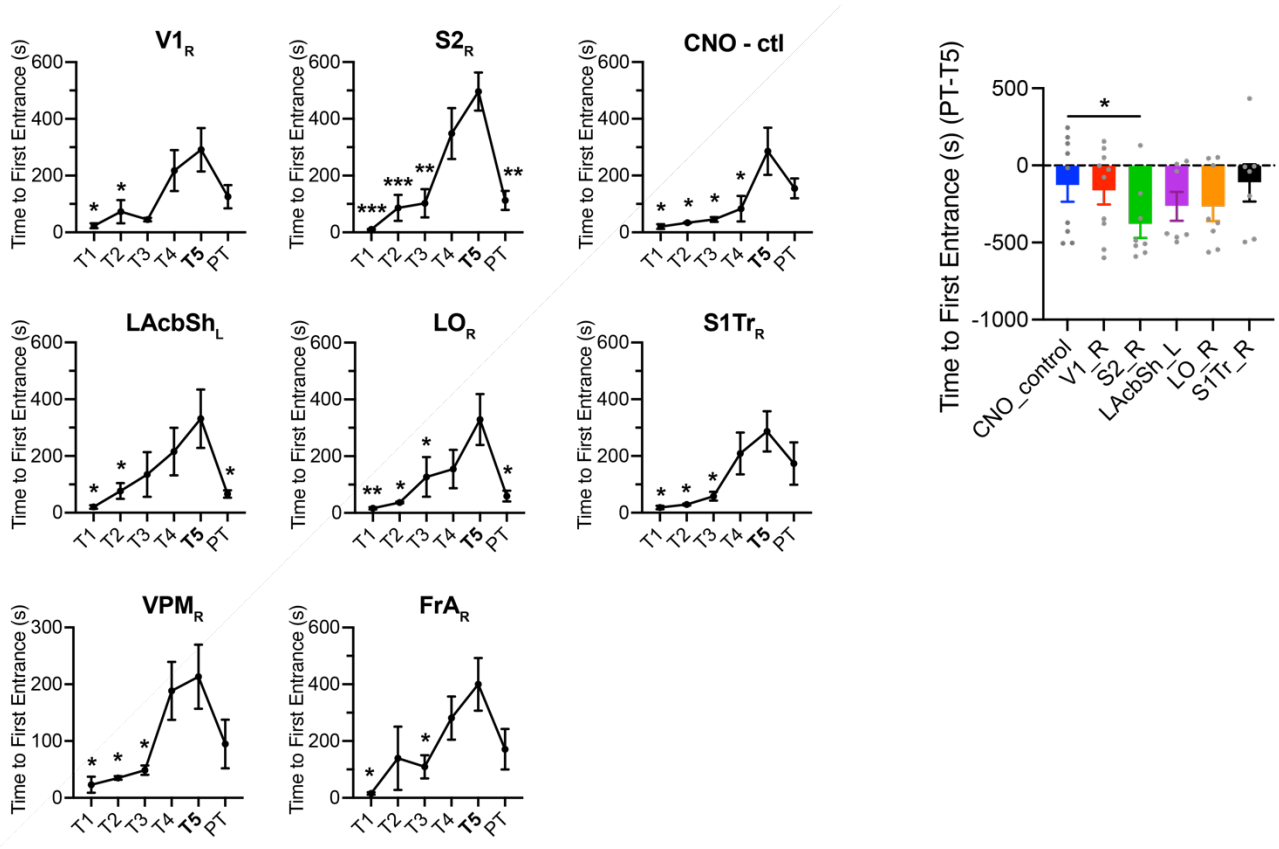

Figure S5 The effect of hub inhibition on the T_{enter}

The left shows the effect of DREADDs inhibition on the T_{enter}. All the comparisons are performed between the last training trial (T5) and other training trials or probe tests. The right shows the comparison of changed T_{enter} (PT – T5) between experimental groups and CNO-control group. One-tail t-test. Data are represented as mean ± SEM. * $p < 0.05$; ** $p < 0.01$; *** $p<0.001$.

Table S1 Behavior correlated functional connections from common networks.
Each row shows the names of the nodes, the behavioral correlation r and p values. $_R$: right hemisphere; $_L$: left hemisphere

		Node 1	Structure name 1	Node 2	Structure name 2	r	p value
Post day 1	N_{shock}	DLG_L	Dorsal lateral geniculate nucleus	$A24b_L$	Anterior cingulate area, dorsal part	-0.72	0.0018
		$CA3\text{-}Or_L$	CA3-Or	$S1BF_L$	Primary somatosensory cortex, barrel field	-0.68	0.0037
		LS_L	Lateral septum	$CA1\text{-}Rad_L$	CA1-Rad	-0.65	0.0069
		$CA2\text{-}Rad_L$	CA2-Rad	STr_R	Subiculum transtion area	-0.58	0.019
		$V1_R$	Primary visual cortex	$S1_R$	Primary somatosensory cortex, unassigned	0.57	0.021
		ADN_L	Anterior dorsal thalamus nucleus	$A24b_L$	Anterior cingulate area, dorsal part	-0.52	0.038
		LP_L	Lateral posterior thalamic nucleus	DEn_L	Dorsal nucleus of the endopiriform	-0.52	0.04
		MN_L	Medial thalamus nucleus	$IPAC_L$	Interstitial nucleus of the posterior limb of the anterior commissure	-0.51	0.041
		$LAcbSh_L$	Accumbens nucleus shell, lateral part	$A24b_L$	Anterior cingulate area, dorsal part	-0.51	0.046
	T_{enter}	$PLTN_L$	Posterior lateral thalamuc nucleus	$Pons_R$	Pons	-0.67	0.003
		$V2MM_L$	Secondary visual cortex: mediomedial area	AuD_L	Secondary auditory cortex, dorsal area	-0.67	0.0033
		$V2MM_L$	Secondary visual cortex: mediomedial area	$Au1_L$	Primary auditory cortex	-0.66	0.0038
		$V1_L$	Primary visual cortex	$MPtA_L$	Medial parietal association cortex	-0.65	0.0044
		GP_L	Globus pallidus	$A30_L$	Retrosplenial area, dorsal part	-0.62	0.0077
		PDN_L	Posterior dorsal thalamus nucleus	$Pons_R$	Pons	-0.61	0.0092
		Sub_L	Subiculum	MB_L	Midbrain	0.6	0.01
		$CA1\text{-}Rad_R$	CA1-Rad	Ce_R	Central amygdaloid nucleus	-0.59	0.012
		$V1_R$	Primary visual cortex	$S1_R$	Primary somatosensory cortex, unassigned	-0.58	0.014
		$CA3\text{-}Rad_L$	CA3-Rad	$V1M_R$	Primary visual cortex, monocular area	0.57	0.018
		MGV_R	Medial geniculate nucleus, ventral part	$CEnt_R$	Caudomedial entorhinal cortex	-0.52	0.031
		$CA1\text{-}Rad_L$	CA1-Rad	$MPtA_R$	Medial parietal association cortex	0.52	0.033
		LTN_L	Lateral thalamus nucleus	$S1HL_R$	Primary somatosensory cortex, hindlimb region	0.51	0.034
		ST_L	Bed nucleus of the stria terminalis	$A24b'_L$	Anterior cingulate area, dorsal part	0.51	0.038
		VPM_R	Ventral postereomedial thalamic nucleus	DLG_R	Dorsal lateral geniculate nucleus	-0.51	0.038
		$LAcbSh_L$	Accumbens nucleus shell, lateral part	$A24b_L$	Anterior cingulate area, dorsal part	0.5	0.042
		LS_L	Lateral septum	$VIEnt_L$	Ventral intermediate entorhinal cortex	0.5	0.042
Post day 8	N_{shock}	$CA3\text{-}Or_L$	CA3-Or	$S2_R$	Secondary somatosensory cortex	-0.8	0.0002
		$AcbSh_L$	Accumbens nucleus shell	$A30_L$	Retrosplenial area, dorsal part	-0.6	0.015
		LS_R	Lateral septum	$MEnt_R$	Medial entorhinal cortex	-0.58	0.02
		Rt_L	Reticular nucleus (prethalamus)	LD_L	Laterodorsal thalamic nucleus	-0.57	0.02
		$LAcbSh_L$	Accumbens nucleus shell, lateral part	$AcbC_L$	Accumbens nucleus core	-0.52	0.038

		$PLCo_L$	Posterolateral cortical amygdaloid area	$CEnt_R$	Caudomedial entorhinal cortex	-0.52	0.041
	$\mathbf{T_{enter}}$	SC_R	Colliculus: superior	AM_R	Anteromedial thalamic nucleus	0.6	0.014
		$APir_L$	Amygdalopiriform transition area	Ce_R	Central amygdaloid nucleus	-0.59	0.015
		Zl_R	Zona incerta	DLG_R	Dorsal lateral geniculate nucleus	0.57	0.02
		PAG_R	Periaqueductal gray	LD_R	Laterodorsal thalamic nucleus	0.55	0.028
		LS_R	Lateral septum	$MEnt_R$	Medial entorhinal cortex	0.54	0.032
		PAG_R	Periaqueductal gray	AM_R	Anteromedial thalamic nucleus	0.51	0.046

Table S2 The number of animals included in each rsfMRI session.

Animals that didn't show visual responses during the fMRI scan were excluded.

Experimental groups	rsfMRI on post day 1	rsfMRI on post day 8
1-Day APA	10 in 12	8 in 12
1-Day control	9 in 12	9 in 12
5-Day APA	7 in 10	8 in 10
5-Day control	5 in 6	5 in 6

Table S3 The ROIs used in seed-based FC analysis.
This ROIs list was used to create the FC matrix. The size of one voxel is 0.2 x 0.2 x 0.2 = 0.008 mm^3.

Abbreviations	Structure name	Number of voxels
A24a	Anterior cingulate area, ventral part	79
A24a'	Anterior cingulate area, ventral part	40
A24b	Anterior cingulate area, dorsal part	72
A24b'	Anterior cingulate area, dorsal part	27
A25	Infralimbic area	29
A29a	Retrosplenial area, ventral part	34
A29c	Retrosplenial area, ventral part	82
A30	Retrosplenial area, dorsal part	106
A32	Prelimbic area	108
AcbC	Accumbens nucleus core	83
AcbSh	Accumbens nucleus shell	77
ADN	Anterior dorsal thalamus nucleus	17
AM	Anteromedial thalamic nucleus	24
Amg	Amygdala	344
APir	Amygdalopiriform transition area	47
APT	Anterior pretectal nucleus	38
Au1	Primary auditory cortex	65
AuD	Secondary auditory cortex, dorsal area	65
AuV	Secondary auditory cortex, ventral area	73
CA1-Lmol	CA1-Lmol	86
CA1-Or	CA1-Or	116
CA1-Rad	CA1-Rad	149
CA2-Rad	CA2-Rad	27
CA3-Or	CA3-Or	207
CA3-Rad	CA3-Rad	80
Ce	Central amygdaloid nucleus	41
CEnt	Caudomedial entorhinal cortex	239
CPu	Caudate putamen	962
CxA	Cortex amygdala transition zones	33
DB	Diagonal band	45
DEn	Dorsal nucleus of the endopiriform	53
DIEnt	Dorsal intermediate entorhinal cortex	87
DLEnt	Dorsolateral entorhinal cortex	118
DLG	Dorsal lateral geniculate nucleus	31
DS	Dorsal subiculum	37
DTT	Dorsal tenia tecta	52
EA	Extension of the amygdala	29
Ect	Ectorhinal cortex	117
FrA	Frontal association cortex	285
GP	Globus pallidus	118

GrDG	Dentate-Gyrus-GrDG	24
Hyp	Hypothalamus	396
IC	Colliculus: inferior	271
IEn	Intermediate nucleus of the endopiriform claustrum	25
Ins	Insular region, not subdivided	317
IP	Interpeduncular nucleus	30
IPAC	Interstitial nucleus of the posterior limb of the anterior commissure	33
LAcbSh	Accumbens nucleus shell, lateral part	25
LD	Laterodorsal thalamic nucleus	37
LH	Lateral hypothalamus	59
LO	Lateral orbital cortex	185
LP	Lateral posterior thalamic nucleus	23
LS	Lateral septum	136
LTN	Lateral thalamus nucleus	20
M1	Primary motor cortex	340
M2	Secondary motor cortex	284
MB	Midbrain	532
MD	Mediodorsal thalamic nucleus	53
MeA	Medial amygdala	36
MEnt	Medial entorhinal cortex	21
MGV	Medial geniculate nucleus, ventral part	24
MM	Mammillary bodies	19
MN	Medial thalamus nucleus	92
MO	Medial orbital cortex	70
MoDG	Dentate-Gyrus-MoDG	245
MPtA	Medial parietal association cortex	20
MS	Medial septal nucleus	30
PAG	Periaqueductal gray	208
PaS	Parasubiculum	70
PBGN	Posterior basal ganglia nucleus	17
PDN	Posterior dorsal thalamus nucleus	70
Pir	Piriform cortex area	470
PLCo	Posterolateral cortical amygdaloid area	35
PLTN	Posterior lateral thalamic nucleus	39
PMCo	Posteromedial cortical amygdaloid area	54
PN	Pontine nucleus	34
Po	Posterior thalamic nuclear group	68
PoDG	Dentate-Gyrus-PoDG	22
Pons	Pons	796
Post	Postsubiculum	32
PRh	Perirhinal cortex	95
PV	Paraventricular thalamic nucleus	16
RAPir	Rostral amygdalopiriform area	17

Re	Reuniens thalamic nucleus	29
Rt	Reticular nucleus (prethalamus)	78
S1	Primary somatosensory cortex, unassigned	184
S1BF	Primary somatosensory cortex, barrel field	433
S1FL	Primary somatosensory cortex, forelimb region	179
S1HL	Primary somatosensory cortex, hindlimb region	125
S1J	Primary somatosensory cortex, jaw region	25
S1Tr	Primary somatosensory cortex, trunk region	33
S1ULp	Primary somatosensory cortex, upper lip region	207
S2	Secondary somatosensory cortex	281
SC	Colliculus: superior	415
SOC	Superior olivary complex	30
ST	Bed nucleus of the stria terminalis	58
STr	Subiculum transition area	71
Sub	Subiculum	20
TeA	Temporal association area	114
Tu	Olfactory tubercle	132
V1	Primary visual cortex	112
V1B	Primary visual cortex, binocular area	84
V1M	Primary visual cortex, monocular area	89
V2L	Secondary visual cortex: lateral area	107
V2ML	Secondary visual cortex: mediolateral area	53
V2MM	Secondary visual cortex: mediomedial area	74
VCl	Claustrum, ventral part	23
VIEnt	Ventral intermediate entorhinal cortex	42
VL	Ventrolateral thalamic nucleus	39
VM	Ventromedial thalamic nucleus	33
VMN	Ventral medial thalamus nucleus	30
VO	Ventral orbital cortex	66
VP	Ventral pallidum	67
VPL	Ventral posterolateral thalamic nucleus	26
VPM	Ventral posteromedial thalamic nucleus	53
Zl	Zona incerta	75